

Evaluating large-domain, hecto-meter, large-eddy simulations of trade-wind clouds using EUREC⁴A data

Hauke Schulz^{1,2}, Bjorn Stevens¹

¹Max Planck Institute for Meteorology, Hamburg, Germany

²University of Washington/CICOES, Seattle, WA, USA

Key Points:

- A 41 days, hm-resolution simulation is run to quantify the ability of ICON-LEM to reproduce the observed cloudiness.
- The simulated cloudiness co-varies with precipitable water, temperature and wind speed mimicking the observations.
- The vertical distribution of cloudiness remains challenging at the cost of representing mesoscale patterns with stratiform cloud amount.

This manuscript is a preprint and has been submitted to the Journal of Advances in Modeling Earth Systems (JAMES) for peer review. As a function of the peer-reviewing process that this manuscript will undergo, its structure and content may change. If accepted, the final version of this manuscript will be available via the 'Peer-reviewed Publication DOI' link on this manuscripts entry on eartharxiv.org.

Corresponding author: Hauke Schulz, haschulz@uw.edu

Abstract

The meso-scale variability in cloudiness of the marine trade-wind layer is explored with large-eddy simulations of regional extent and validated against observations of the EUREC^{4A} field campaign. 41 days of realistically forced simulations present a representative, statistical view on shallow convection in the winter North Atlantic trades that includes a wide range of meso-scale variability including the four recently identified patterns of spatial organization: *Sugar*, *Gravel*, *Flowers* and *Fish*. The results show that cloud cover is on average captured well but with discrepancies in its vertical and spatial distribution. Cloudiness at the lifting condensation level depends on the model resolution with the finer one producing on average a more realistic cloud profile. Independent of the resolution, the variability in cloudiness below the trade inversion is not captured, leading to a lack of stratiform cloudiness with implications on the detectability of meso-scale patterns whose cloud patches are characterized by stratiform clouds. The simulations tend to precipitate more frequently than observed, with a narrower distribution of echo intensities. The observed co-variability between cloudiness and environmental conditions is well captured.

Plain Language Summary

Clouds generally cool the planet due to their ability to reflect sunlight efficiently. To estimate this cooling in a future climate, the processes leading to cloud formation need to be understood. A process that current climate simulations struggle to capture due to their coarse resolution is the variability and patterning of cloudiness on scales on the order of 10-100km. In this study we ran higher resolved simulations at hm-resolutions by limiting the region to the downstream North Atlantic trades where the patterning of shallow clouds is common. Coinciding our simulations with the measurements of the EUREC^{4A} field campaign and being able to run them for over a month allowed us to pin-point current deficits that these higher resolved simulations have. These are in particular the vertical cloud distribution with too little stratiform cloud amount and too much precipitation that hardly changes with the patterning in cloudiness. Nevertheless, the simulations do a good job in capturing the day-to-day variability in total cloud cover and its co-variability with environmental conditions justifying a further study of the phenomenon with these kind of simulations and ultimately improving the climate simulations on this aspect.

45 **1 Introduction**

46 Clouds associated with shallow maritime convection have been recognized as a vi-
47 tal contributor to the net cloud radiative effect for decades (Bony & Dufresne, 2005, Hart-
48 mann et al., 1992). Both small areas with large cloud fractions and large areas with small
49 cloud fractions, make important contributions to these effects. The eastern ocean basins,
50 where cold ocean currents and the overlying warm air give rise to extensive cloud decks,
51 is an example of a small area with a large coverage of clouds. The trade-wind regions
52 typify the idea of a large region with a relatively small coverage of clouds. Often these
53 limiting cases are idealized as end points of a continuous transition, as overcast regions
54 break-up into scattered, randomly distributed, cumulus convection as air-masses are ad-
55 vected over warmer waters by the trade winds.

56 Nature is more messy, as even in the downwind trades cloudiness can vary consid-
57 erably, something that Riehl (1954) already pointed out. And although scattered, seem-
58 ingly random, distributions of rather shallow clouds, are observed in the downstream trades,
59 the prevalence of such cloud regimes might have been over-emphasized by modeling stud-
60 ies on domains too small to capture meso-scale forms of organization (Siebesma et al.,
61 2003, vanZanten et al., 2011). As more modern observations began documenting vari-
62 ability in the forms of organization of clouds in the trades (Rauber et al., 2007), and it
63 became possible to simulate clouds using fine-meshes on larger (but still not particularly
64 large) domains (Heus & Seifert, 2013), attention began to focus on what determines how
65 shallow convection organizes, and how this influences cloud amount (Bretherton & Blossey,
66 2017).

67 More recently, research has demonstrated that variations in cloudiness in the down-
68 stream trades can often be associated with recognizable meso-scale patterns (Stevens,
69 Bony, et al., 2020), and how these patterns help explain differences in cloud-radiative ef-
70 fects (Bony et al., 2020). Using observations, Schulz et al. (2021) has further demonstrated
71 that these patterns encompass different cloud morphologies which emerge in association
72 with distinct meteorological environments. These findings support the idea that changes
73 in cloud amount with warming might be realized by a different selection of large-scale
74 conditions, and hence a change in the mix of mesoscale cloud patterns, a possibility that
75 is all the more intriguing because state-of-the-art climate models do not account for this
76 variability (Nuijens et al., 2015).

77 To understand the factors that influence clouds in the trades, Large Eddy Simu-
78 lation is a useful tool; all the more because advances in computing now make it possi-
79 ble to perform relatively fine mesh simulations over very large (ca. 1000 km) domains
80 for periods of days (Stevens, Acquistapace, et al., 2020) to weeks. In addition, new mea-
81 surement techniques and associated data sets have simultaneously been developed which
82 make it possible to critically and quantitatively assess the fidelity of the simulations, and
83 hence the appropriateness of the tool. Exemplary of the new data sources are the EUREC^{4A}
84 measurements, which were collected to, in part, "provide a reference data-set that may
85 be used as a benchmark for the modelling and the satellite observation of shallow clouds
86 and circulation" (Bony et al., 2017). To accomplish this objective a very large number
87 of both complementary and redundant cloud observations were assembled during EUREC^{4A}.
88 The campaign also made use of extensive soundings (2614 soundings were dropped or
89 launched in total) in ways that allowed to characterize the meso-scale (200 km) environ-
90 ment (Bony & Stevens, 2019) upwind of the Barbados Cloud Observatory (Stevens et
91 al., 2021), as well as an enormous wealth of in situ data, satellite and surface based re-
92 mote sensing. Capitalizing on these data a few recent studies (Dauhut et al., 2023, Naren-
93 pitak et al., 2021) have begun to explore factors influencing the mesoscale organization
94 of clouds, albeit from the point of view of cloud structures that span hundreds of kilo-
95 meters, over still relatively small (200 km) domains, and with varying degrees of quan-
96 titative assessment.

97 In this paper we use a subset of the EUREC^{4A} measurements to evaluate more broadly
98 the ability of numerical simulations, with fine (156 m to 624 m) grids, to quantitatively
99 represent the observed cloud fields and their co-variability with their meso- to large-scale
100 environment over much larger domains, and by using a much larger cross section of the
101 EUREC^{4A} data. This allows us to ask:

- 102 1. To what extent do the simulations capture the mean features of the observed cloud
103 field?
- 104 2. How well do the simulations reproduce the observed variability in cloudiness, par-
105 ticularly in relation to meso-scale patterns of cloudiness and its co-variability with
106 the meteorological environment.

107 In addressing these questions we highlight the strengths and weaknesses of state-
108 of-the-art LES, and identify the limitations that future work must overcome to get the

109 most out of the technique. We proceed as follows: Section 2 describes the simulation con-
110 figurations, observations and the forward operators used to better compare the simula-
111 tion output with measurements. Section 3 discusses the similarities of cloudiness in Large
112 Eddy Simulation (LES) and observations. We conclude with Section 4.

113 **2 Data and Methods**

114 **2.1 Simulations**

115 We focus on the downwind trades of the North Atlantic during January - Febru-
116 ary 2020, a period when this area has been intensively sampled as part of the EUREC⁴A
117 field campaign (Stevens et al., 2021). We conducted simulations with the ICOSahedral
118 Nonhydrostatic (ICON) model family (Dipankar et al., 2015, Gassmann, 2013, Wan et
119 al., 2013, Zängl et al., 2015) at grid spacings of 1.25 km (ICON-SRM), 624 m (ICON-624m),
120 312 m (ICON-312m) and 156 m (ICON-156m). With the exception of the storm-resolving
121 simulation (ICON-SRM), which is used for the initialization and to provide lateral bound-
122 ary conditions for the finer mesh, all simulations are based on the large-eddy simulation
123 capabilities as in Heinze et al. (2017). This branch of the model is called ICON-LEM
124 in the remainder of the manuscript.

125 The configuration of the different simulation domains, and how they are forced is
126 summarized with the help of Table 1. The ICON-LEM domains (Fig. 1) are extended
127 in the east-west direction to better align with the trade-winds and thereby maximize the
128 temporal coverage of the evolution of the shallow convection. The eastern boundaries
129 of the nested domains decrease with each refinement by at least two degrees to reduce
130 the possibility of numerical artifacts entering the domain with the prevailing easterly trades
131 and allow for spin-up of the small-scale turbulence. On the western boundaries less of
132 a margin is provided, as inflow from the west only occurs at upper levels, and thus at
133 most affects high-clouds, which were infrequent and showed little sign of influencing low-
134 level cloudiness.

135 The simulations were designed so that even the smallest (ICON-156m) domain would
136 be large enough to capture meso-scale variability in its full extent, including all four of
137 the mesoscale patterns observed and defined by Stevens, Bony, et al. (2020). As such the
138 ICON-156 domain extends over 9.75° of longitude and 5.00° of latitude, and thereby cov-
139 ers an area spanning about 1050 km in the east-west direction, and 550 km from the south

Table 1. Overview about used simulation configurations.

Model	ICON-SRM	ICON-624m	ICON-312m	ICON-156m
Timeperiod (m/d HH)	1/7 - 3/1	1/9 10 - 2/19 10	1/9 16 - 2/19 10	2/1 06 - 2/8 00
No. grid cells x levels	6773696 x 75	4528560 x 150	11792076 x 150	24469588 x 150
hor. grid spacing*	1248 m	624 m	312 m	156 m
ver. grid spacing (lowest level/ 1000 m/ 2000 m)	20 / 140 / 190 (150 levels)	20 / 70 / 85 (150 levels)	20 / 70 / 85 (150 levels)	20 / 70 / 85 (150 levels)
Model top (km)	35	21	21	21
hor. domain	67W - 43W, 0N-24N	60.25W - 45W, 7.5N - 17N	60W - 47W, 9N - 16.25N	59.75W - 50W, 10.5N - 15.5N
Forcing (except SST)	ECMWF IFS (hourly) ⁺	hourly ICON-SRM	continuously (linear interp. from 1h ERA5 SKT)	one-way online nesting
Forcing (SST)	ECMWF IFS (fixed at initial time)			
restart	daily at 00 UTC			
Turbulence	turbulent kinetic energy (TKE)		none	
Microphysics	One moment incl. graupel (Baldauf et al., 2011)		Smagorinsky diffusion	
Cloud-scheme	Fractional cloud cover		Two moment (Seifert & Beheng, 2006)	
Radiation		RRTM (Mlawer et al., 1997, Stevens et al., 2013)	All-or-nothing	

* edge lengths of triangular grid cells

⁺ analysis at 00:12 UTC ; otherwise IFS forecast

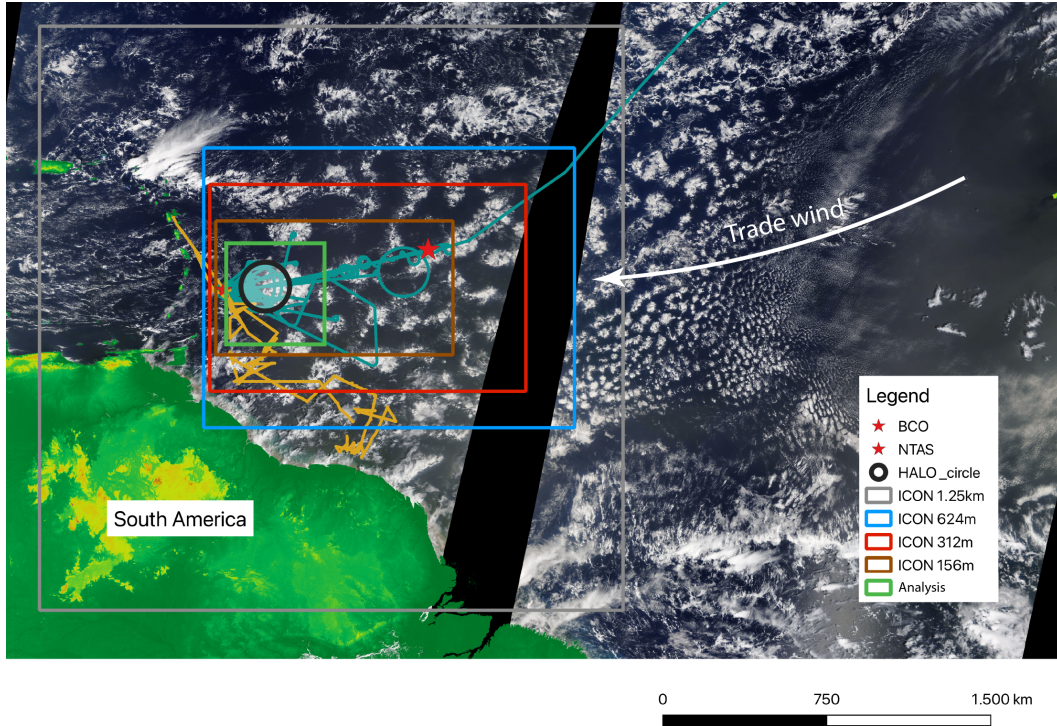


Figure 1. Overview of simulation domains ICON-SRM (gray), ICON-624m (blue), ICON-312m (red), ICON-156m (brown). The tracks of the research aircraft HALO and R/V L'Atalante, which are representative for the two different measurement foci of the EUREC⁴A campaign are shown in orange and teal, respectively. EUREC⁴A-circle is shown in black. The location of the BCO and the NTAS buoy are marked with a red star at the western and eastern part of the domain, respectively. For a sense of scale, the MODIS image of February 12 is shown with land-masses colored in green to brown depending on height. The analysis domain is highlighted in green, well removed from effects of upstream boundaries.

140 to the north. This makes our finest-grid domains slightly larger than the fine-grid do-
 141 main used by Heinze et al. (2017) and several times larger than the expected (ca. 200 km)
 142 size of the meso-scale structures we look to represent – as is also evident, for instance,
 143 in Fig. 1. For the analysis itself a common domain from 11° N - 15° N and 59.3° W - 55.3° W
 144 is used to reduce influences of the boundary conditions if not stated otherwise. If results
 145 do not change significantly with resolution, only the ICON-312m analysis is displayed.

146 The simulations were created as follows. First, the ICON-SRM simulations were
 147 performed to provide initial and boundary conditions for the LES. The ICON-SRM sim-
 148 ulation were initialized daily from the IFS for the period between 9 January and 19 Febru-

149 ary and run for 40 h, with hourly boundary conditions taken from the IFS that assim-
150 ilated available EUREC⁴A observations. The last 24 h of each of these 40 h forecasts were
151 then used to provide lateral boundary condition for the continuously running ICON-624m
152 simulation, which then provided lateral boundary conditions for a one-way nested ICON-
153 312m simulation, and so on.

154 For the lower boundary, sea skin temperatures were updated every timestep based
155 on linearly time-interpolated hourly ERA5 skin temperatures. Skin temperatures were
156 chosen over SST because ICON does not have a skin temperature parameterization and
157 the usage of SST would introduce a warm bias assuming the ERA5 skin temperatures
158 are accurate. However, there is a possibility that the ERA5 skin temperatures are too
159 cold due to a cold bias of the ERA5 sea surface temperatures, which they are based upon.
160 Compared to the SST measured by the research vessel Meteor (R/V Meteor), the ERA5
161 SST is on average 0.4 K colder. The use of the skin-temperature introduces another 0.2 K
162 suppression.

163 If the cool skin-temperature estimated by the surface flux schemes used by the ERA5
164 over-states this effect (and there are some indications that it does) this could result in
165 the SSTs being as much as 0.6 K colder than observed. A comparison of SSTs measured
166 by the R/V Ronald H. Brown, and Saildrones, which operated on an area beyond the
167 EUREC⁴A-circle, showed biases ranging from -0.4 K to $+0.2\text{ K}$ (Wick et al., 2023), putting
168 our estimates of biases near the cold end of what they record. Attempting to correct these
169 biases is however difficult, as doing so introduces the possibility of introducing inconsis-
170 tencies with the lateral boundary conditions and pressure gradients of the re-analysis.
171 For this reason we simply note the discrepancy and return to its possible effects in the
172 context of analyses where it might have some bearing on the results.

173 The above procedure required the ICON-LEM simulations to be initialized only
174 once. The ICON-624m was initialized at 10 UTC on January 9th, and then used to ini-
175 tialize the ICON-312m 6 h later. Output after midnight of January 10, 2020 until Febru-
176 ary 19 is used in the analysis, totaling to 40 analysis days.

177 The method chosen for specifying the lateral boundary conditions for the ICON-
178 624m simulations introduces a discontinuity at 16 UTC during the transition from one
179 day's ICON-SRM forecast to the next days. This discontinuity is expected to be small
180 – indeed we see no apparent impact of this daily 're-alignment' of the boundary condi-

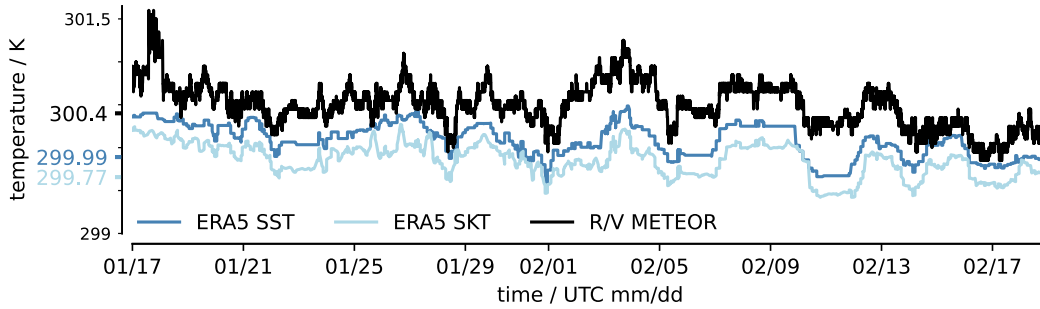


Figure 2. Comparison of the simulation’s surface boundary conditions based on ERA5 skin-temperatures (SKT) to ERA5 foundation temperatures (SST) and measurements taken on-board the R/V Meteor at a depth of 2.1 m. For better comparison the nearest grid-cells of the model to the ship’s track along its north-south transects (12.1° to 14.5° N) at 57.245° W are used. Note that the sub-daily variations of ERA5 SSTs are caused by this sampling strategy and are constant in space and time within a day.

181 tions in our analysis – as the ICON-SRM is continually updated by the analysis at its
 182 lateral boundaries. Re-initializing the ICON-SRM each day, however, helps ensure that
 183 the large-scale conditions, and hence the lateral boundary conditions provided to the ICON-
 184 624m simulation, remain well aligned with what was observed.

185 An additional nest at 156m grid spacing, ICON-156m, is included for the period
 186 of February 1 to February 7 to oppose *Sugar* and *Flowers* at even higher horizontal res-
 187 olutions, as it will turn out ICON-LEM has problems to distinguish these patterns. The
 188 roughly ten-fold greater computational intensity of this configuration precluded a longer
 189 simulation.

190 *2.1.1 Satellite forward simulator*

191 To compare the mesoscale variability and horizontal structure of the cloud field,
 192 we use infrared satellite imagery. To retrieve consistent fields from the simulations, we
 193 rely on the RTTOV forward simulator (Saunders et al., 2018) to emulate satellite im-
 194 ages. In this study, we use the Geostationary Operational Environmental Satellite (GOES)-
 195 16 Advanced Baseline Imager (ABI) specifications to compare them to the actual satel-
 196 lite’s instrument, which covers the region of interest with a high temporal and spatial
 197 sampling of 10 min and 2 km (channel 13: $10.35\ \mu\text{m}$), respectively. In an attempt to get

198 the most consistent synthetic satellite images, we made modifications to the most recent
 199 version of ICON (2.6.3). These modifications include design changes that let us use RT-
 200 TOV v13 during the run time of ICON and reduce the amount of output that needs to
 201 be saved to disk for offline calculations. In addition, we use the calculated two-moment
 202 microphysics to feed both the internal RRTM radiation scheme and the one of RTTOV
 203 to make their input consistent.

204 The synthetic satellite images are calculated every 10 minutes to match the tem-
 205 poral resolution of the ABI instrument. A snapshot of the animation ([https://doi.org/
 206 10.5281/zenodo.7567204](https://doi.org/10.5281/zenodo.7567204)) that visualizes the actual and synthetic satellite images for
 207 the complete time period is shown in Fig. 3.

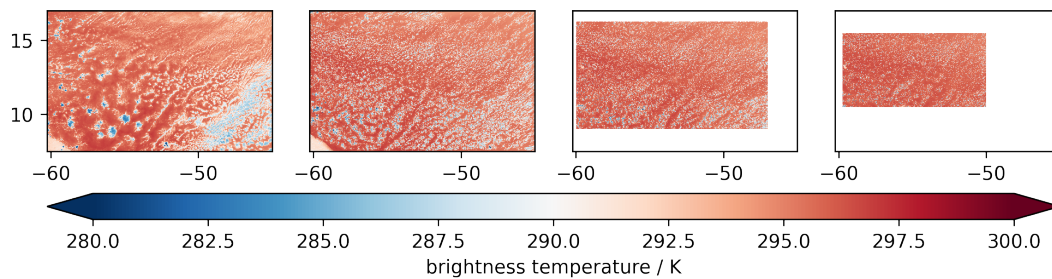


Figure 3. Snapshot of GOES-16 ABI channel 13 satellite image (left) and the synthetic counterparts from ICON-624m, ICON-312m and ICON-156m (from left to right) for February 2, 2020 at 7:50 UTC. Full animation available at <https://www.doi.org/10.5281/zenodo.7567204>.

208 *2.1.2 Radar forward simulator*

209 Past work has emphasized how the trade-wind boundary layer is sensitive to the
 210 distribution of cloudiness in the vertical (Brient et al., 2016, Nuijens et al., 2014, Vogel
 211 et al., 2022). Likewise, different patterns of mesoscale variability have been shown to be
 212 associated with different vertical profiles of cloudiness (Schulz et al., 2021), but past work
 213 suggests that it proves difficult for simulations to robustly capture this structure (At-
 214 las et al., 2020, Stevens et al., 2001) even when not conditioned on different patterns of
 215 cloudiness.

216 Hence in evaluating the fidelity of ICON-LEM we also compare the vertical pro-
 217 files of the simulations to observations. For this purpose we use a forward simulator to
 218 resemble the vertical distribution of cloudiness as seen by the Ka-Band radar positioned

219 at the Barbados Cloud Observatory (BCO) (see next section), as this is well situated at
 220 the downstream end of our domain, and was also used in the study by Schulz et al. (2021).

221 We rely on the radiative transfer simulator PAMTRA (Passive and Active Microwave
 222 TRANsfer package) (Mech et al., 2020) as it has successfully been used with the same
 223 radar frequency in earlier studies in this region (Jacob et al., 2020). PAMTRA has been
 224 configured similar to Mech et al. (2020) to be consistent with ICON-LEM’s representa-
 225 tion of cloud microphysical processes. Hence, PAMTRA is able to infer the original par-
 226 ticle size distribution assumed by the simulations from its bulk measures of mixing ra-
 227 tio and number concentration, which are saved every 60 s at the location of the BCO.
 228 PAMTRA therefore simulates reflectivities that are nominally consistent with the mi-
 229 crophysical state of the LES. Although the higher moments of the hydrometeor distri-
 230 bution are not strongly constrained by the bulk schemes used to model cloud microphysics,
 231 our use of the PAMTRA based reflectivities is limited to the creation of a rain and cloud
 232 mask, which should limit the impact of ambiguities in the forward model.

233 **2.2 Observations**

234 **2.2.1 EUREC⁴A Observations**

235 Among the tremendous amount of observation platforms that were present in the
 236 simulated area during the EUREC⁴A time period, the Barbados Cloud Observatory (BCO),
 237 was a fixed point. The BCO is situated at Deebles Point, a windward promontory on
 238 Barbados (Stevens et al., 2016), an island situated near the western boundary of our sim-
 239 ulation domains. We used the measurements from the BCO’s vertically pointing Ka-band
 240 radar CORAL to detect the vertical distribution of hydrometeors. Averaging these mea-
 241 surements in time results in echo fractions which are a combined measure of cloud frac-
 242 tion and precipitation fraction. A threshold of -50 dBZ has been applied to exclude backscat-
 243 ter from deliquesced large sea-salt aerosols near the lifting-condensation level (Klinge-
 244 biel et al., 2019).

245 Measurements from radiosondes launched from the BCO and ships, as well as ex-
 246 tensive (1068) dropsondes launched from research aircraft along the EUREC⁴A-circle (up-
 247 wind of the BCO, as shown in Fig. 1)(George et al., 2021) were integrated into the global
 248 observation system to help constrain the large-scale analysis, e.g. in the set-up of this
 249 study. In the past, there had been the concern that the large-scale vertical winds from

250 the reanalysis winds would not be representative of the observed conditions. George et
 251 al. (2022) demonstrates that the mean large-scale vertical motion observed across the
 252 EUREC⁴A-circle agrees well with the analysis, also when the sondes were not included,
 253 giving confidence in the ability of the analysis to capture the large-scale conditions and
 254 provide representative boundary conditions of the ICON-SRM run.

255 EUREC⁴A featured a wide variety of surface, air-born and ship-based radars and
 256 lidars as well as passive information (Stevens et al., 2021), which could be used for more
 257 detailed studies, but for this first evaluation we focus on a comparison with the BCO data,
 258 as it is sufficient to identify the main issues.

259 **2.3 Classifications of meso-scale patterns**

260 Two approaches to identify the meso-scale patterns of shallow convection are in-
 261 troduced. First, for identifying the days with observed canonical meso-scale patterns,
 262 we rely on the manual classifications done by the scientific community of the EUREC⁴A
 263 field campaign as described in Schulz (2022). The scientists inspected satellite images
 264 captured during the EUREC⁴A time period and labeled regions containing *Sugar*, *Gravel*,
 265 *Flowers* or *Fish*. The result of the classification based on infrared satellite images for
 266 the analysis region, by day, is shown in Fig. 4. A day is associated with a particular type
 267 if at least 40% of the scientists have assigned a specific pattern to the region. If the frac-
 268 tion is below 40% or several patterns have been detected, the day contains *mixed* mesoscale
 269 cloud patterns.

270 These pattern days are used to sub-sample the simulations so as to test their abil-
 271 ity to match the characteristics of the observations in conjunction with the observation
 272 of specific patterns.

273 Second, we classified the simulations themselves to test whether the frequency of
 274 patterns matches with the one observed but differs in phase. For this purpose, we clas-
 275 sified also the observations again, using the neural network that has been successfully
 276 used in Schulz et al. (2021). The neural network has been trained to detect the cloud
 277 patterns in GOES-16 ABI infrared images and classifies in each input image regions that
 278 contain a particular pattern. To apply the neural network to the simulations we used
 279 the 10 min output of the RTTOV forward simulator as discussed above. The results of
 280 these classifications are shown in detail in Fig.S1.

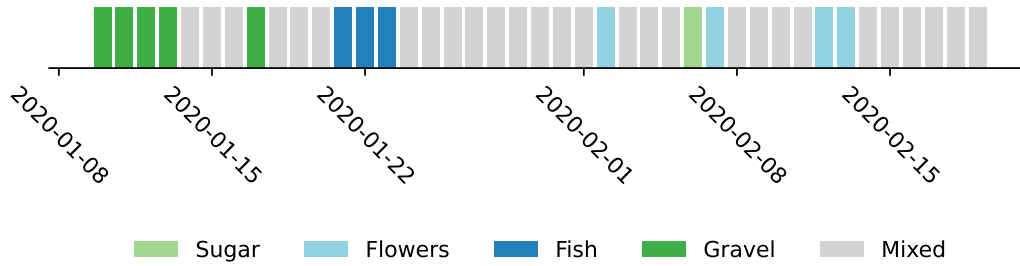


Figure 4. Prevailing meso-scale patterns identified by the EUREC⁴A community in GOES-16 ABI infrared satellite images (Schulz, 2022), here shown for the analysis region.

3 Similarity of LES and observations

3.1 Characterisation of environment

Variability in the atmospheric environment is thought to influence the development of different meso-scale patterns of cloudiness. For instance, Schulz et al. (2021) demonstrated that anomalously warm air-masses, which tend to originate from lower latitudes, and result in shallower cumulus clouds (with a vertical extent of a couple of 100 meters) more likely to be classified as *Sugar*. Anomalously cool air masses tend to originate from higher latitudes, and depending on factors such as the strength of the subsidence or the near-surface wind-speed, align with other meso-scale patterns of cloudiness. Thus, in what follows we not only explore to what extent the LES represents the observed structure of the lower troposphere, and in particular its variability in association with different meso-scale patterns of cloudiness.

Fig. 5 illustrates the atmospheric boundary layer, its variability within the simulated period, and how it co-varies with meso-scale patterns of cloudiness as identified by the satellite imagery. As such it presents a representative picture of the winter-time trade-wind boundary layer as captured by the large-eddy simulation during the period of EUREC⁴A. The simulated profiles of specific humidity, potential temperature, and wind-speed are broadly similar to the vertical structure as sampled by the research aircraft across the EUREC⁴A-circle. The observations and simulations document a moist layer of 1.5 km to 3.5 km with elevated wind speeds, and a well mixed sub-cloud layer below about 600 m. On average the simulations show a 1 K cooler and 1 g kg^{-1} drier moist layer, with slightly stronger wind speeds through the bulk of the cloud layer. The reduction

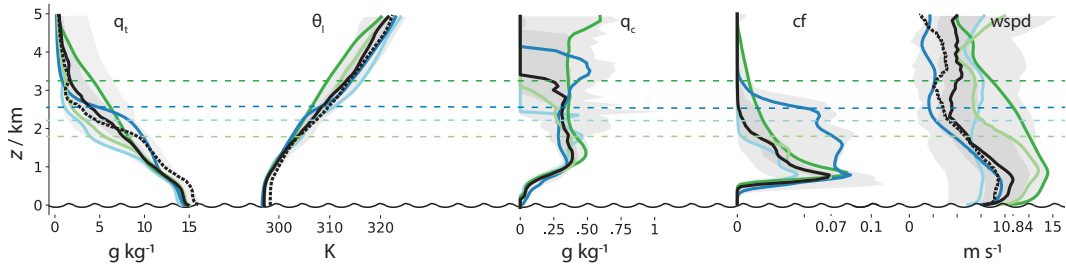


Figure 5. Variability of the simulated trade-wind boundary layer illustrated by median (black profile) and minimum/maximum (light grey) and 25/75th percentile (dark grey) of daily median profiles for total water specific humidity (q_t), liquid water potential temperature (θ_l), cloud water specific mass (q_c , averaged over cloudy points only), cloud fraction (cf, def. as $q_c > 0$) and wind speed. Profiles of days with clear meso-scale organization are indicated by colors following the scheme of Fig. 4: *Fish* (January 22), *Flowers* (February 2), *Gravel* (January 12), *Sugar* (February 6). The levels of maximum θ_l gradient (inversion height) are indicated with a dashed line. For a better comparison with the median profile of the campaign’s dropsondes (dashed) that were dropped along the EUREC⁴A-circle from the *HALO* (*High Altitude and Long Range Research Aircraft*)(George et al., 2021), only the encircled area has been analysed for this figure.

303 in specific humidity in the simulations is consistent with what would be expected were
 304 the relative humidity unchanged.¹. In addition to being absolutely drier, and cooler, the
 305 simulations show a more continuous transition between the top of the sub-cloud layer
 306 at 600 m and the free troposphere (near 3000 m). The soundings document a stronger
 307 hydro-lapse, at about 2 km, and a better mixed cloud layer between 600 m to 1500 m.

308 Systematic biases can be better quantified by comparing the meteogram output from
 309 the LEM with near surface observations from the R/V Meteor. Fig. 6 provides such a
 310 comparison for the near surface temperature, humidity and wind-speed. By comparing
 311 to the R/V Meteor measurements, we avoid possible distortion associated with the ef-
 312 fect of the promontory on which the BCO measurements are situated, and temporal sam-
 313 pling biases, but must contend with the fact that the R/V Meteor moved north and south
 314 along a constant line of longitude within the eastern part of the EUREC⁴A-circle, while
 315 the meteogram output was situated a bit to the east, at a fixed position, near the east-

¹ The difference in the specific humidity for a 1 K temperature increase of air at 300 K with a fixed relative humidity of 75 % and a pressure of 1015 hPa is 1 g kg^{-1} .

316 ern edge of the circle. The comparison confirms the ca. 1 K temperature bias, with a some-
 317 what less pronounced tail toward colder temperatures potentially indicative of less cold-
 318 pool activity. The simulated near surface relative humidity is slightly higher than ob-
 319 served, but this might result from a poor resolution of the surface layer. Wind-speeds
 320 near the surface are also slightly reduced as compared to the observations, in contrast
 321 to what is observed in the bulk of the boundary layer. The day-to-day variability of wind-
 322 speed is however captured in contrast to relative humidity and temperature that vary
 323 too little (Fig. S3).

324 Comparing only the circle-median profiles of the simulations with the soundings
 325 during flight days, the thermodynamic structure above 2000 m agrees better, but the main
 326 bias below 2000 m remains. Focusing on the 1 Feb. to 7 Feb. period, which was also sim-
 327 ulated with ICON-156m, showed that 1 K to 1.2 K cold-biases were apparent in the sub-
 328 cloud layer on all three flight days (2, 5 and 7 Feb) but 1.0 g kg^{-1} to 1.5 g kg^{-1} dry and
 329 -0.5 m s^{-1} to 0.5 m s^{-1} wind biases were only evident for the first two of these days (not
 330 shown). In both cases (2 and 5 Feb) the simulated cloud layer was shallower than ob-
 331 served. There is a notable and systematic reduction in the wind-speed bias as the grid
 332 spacing was refined from 623 m to 156 m, but no systematic improvement in the ther-
 333 modynamic structure.

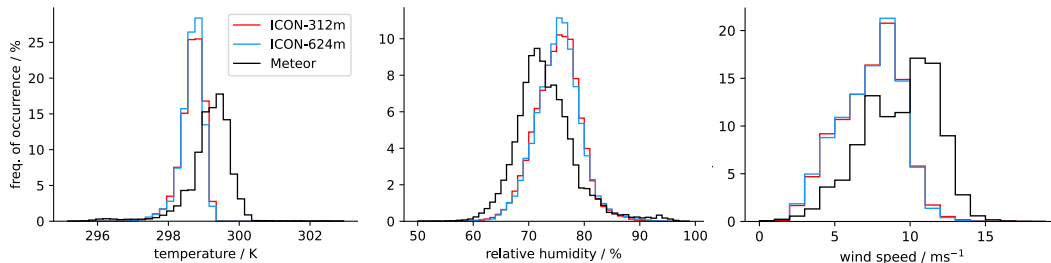


Figure 6. Histograms of temperature (left), relative humidity (middle) and wind speed (right). The observations are based on measurements from the R/V Meteor during its north-south transects at about 57.245°W from 12.1° to 14.5°N . The simulation's quantities are based on the meteogram output at 13.3°N , 56.717°W (eastern circle edge).

334 The persistence of the cold bias could, in part, be explained by the sea-surface tem-
 335 peratures being prescribed as too cold. Compared to the R/V Meteor measurements,
 336 it is hard to make the case for more than a 0.6 K cold bias in the surface temperatures

(Fig. 2), which is less than half of the bias in near surface air-temperatures, hence other factors seem to be involved. Even with all observations from EUREC⁴A assimilated, the cold and dry bias of about 1 K and 1 g kg^{-1} remains in the ERA5 reanalysis. That the biases are evident for the 2-5 Feb. period helps isolate this time-period for more intensive analysis, perhaps also in comparison with the mixed layer budgets derived from the sounding data by Albright et al. (2022).

Analysis of the different days shows that large changes in the structure of the cloud layer are apparent, as in the observations. The maximum gradient in liquid water potential temperature can vary between 1.5 km to 3.5 km on timescales of several hours. These differences are also evident in Fig. 5. To some extent the variability is consistent with environmental variations previously noted in association with the differing cloud patterns, with shallower moist layer for *Flowers* and *Sugar*, stronger near surface winds for *Gravel* and increased lower-tropospheric stability in the case of *Flowers*. The *Fish* pattern (January 22) is largely influenced by the cloudy part and to a smaller extent by the clear-sky region. The discrepancy that stands out the most is in the representation of *Flowers* (e.g., February 2) where the simulated cloud fraction is much smaller than observed.

3.2 Meso-scale patterns

3.2.1 Visual inspection

To evaluate the ability of the simulations to capture the mesoscale patterning of the atmosphere we first visually inspect the spatial distribution of clouds, as was done to identify the cloud patterns in the original studies (e.g., Rasp et al., 2020, Stevens, Bony, et al., 2020). In the case of the simulated cloud scenes the visualization is based on the RTTOV output. These simulated scenes are compared to satellite scenes observed at the same time in Fig. 7.

This comparison demonstrates that most of the scenes match the general structure of the patterns with the exception of *Flowers*.

The simulated structures of *Fish* and *Gravel* align best with observations of the same patterns, as shown in Fig. 7a. *Fish* shows band structures of cloudy and clear-sky patches and *Gravel* consists of much smaller patches that are roughly arranged in hexagons.

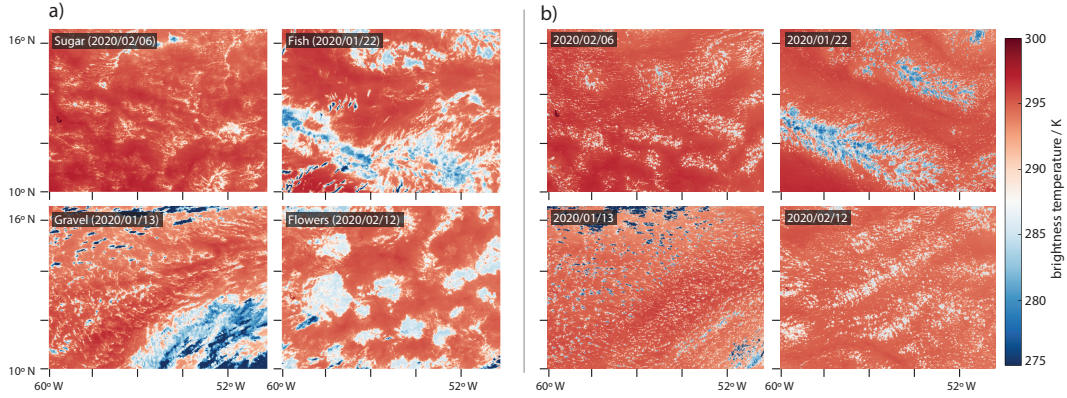


Figure 7. Meso-scale patterns of shallow convection in the trades as defined by Stevens, Bony, et al. (2020) and observed in Moderate Resolution Imaging Spectroradiometer ABI images (left) and their simulated counterpart based on ICON-312m matching the same times and regional extent (right). Visualized is the brightness temperature of channel 13 (10.18 μm to 10.48 μm).

367 Some clouds also rise deeper and produce stratiform clouds that are also visible for this
 368 day in the observations. The 2-m-temperature field (not shown) also confirms the fre-
 369 quent and wide-spread occurrence of cold pools as are often associated with the cloud-
 370 arcs evident on days when these patterns are evident.

371 Simulated *Flowers* are, however, not readily distinguishable from the *Sugar* scene
 372 in the simulations. The main deficiency appears to be the failure of the simulations to
 373 reproduce the stratiform layers observed in association with *Flowers*. This deficiency is
 374 not remedied by a factor of four refinement in the horizontal grid (see supplemental Fig.
 375 S2), as differences between the ICON-624m and the ICON-156m simulations are still sub-
 376 stantially smaller than between the finest resolution simulations and the observations.
 377 Past work (Stevens et al., 2001), using more idealized configurations suggest that the de-
 378 velopment of stratiform layers is quite sensitive to the numerical methods used in both
 379 the momentum and scalar transport, rendering the ability of LES to differentiate among
 380 the ability of different cloud environments to develop stratiform cloud layers as a crit-
 381 ical and challenging test of the method.

382 **3.2.2 Fractional coverage from neural networks**

383 To objectively describe the capability of the simulations to represent the spatial
 384 distribution of cloud patches as meso-scale cloud patterns, the synthetic satellite images

385 are also classified by the neural network of Schulz et al. (2021). By comparing these clas-
 386 sifications with those based on satellite observations, the short-comings of the simula-
 387 tion become more apparent.

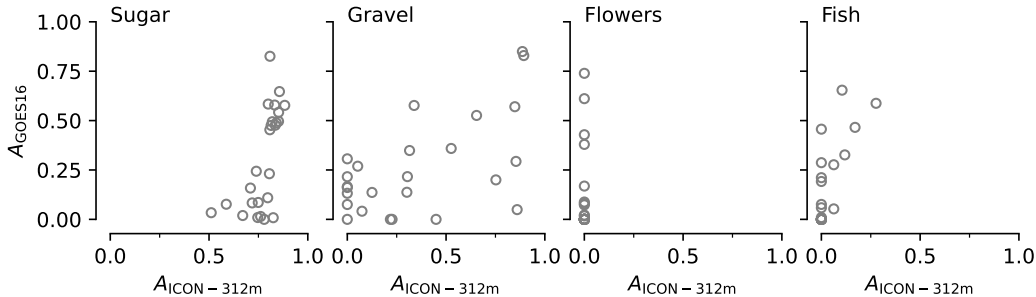


Figure 8. Daily mean area fraction covered by meso-scale patterns as identified by the neural network on actual (ABI) and simulated (ICON-312m) satellite images. 14 days containing high clouds are excluded.

388 Fig. 8 shows the agreement in daily area fraction A of a particular pattern as iden-
 389 tified in the simulation and the observations. Here we use the domain of ICON-156m (7.5N-
 390 17N and 60.25W-45W) as a common domain to improve the sampling. A repetition of
 391 the analysis on the smaller domain was noisier, but in qualitative agreement (not shown).
 392 The inference from the previous section that *Sugar* is too widespread can be confirmed
 393 by this analysis. Day-to-day variability in the area coverage of *Sugar* is much less in the
 394 simulations. It is present in nearly 80 percent of the domain on all days. In the obser-
 395 vations, and in contrast, the area fraction ranges between 0% and 80%. This appears mostly
 396 compensated for by *Flowers*, which are not identified in the simulations, but are not in-
 397 frequent, and on some days quite pronounced, in the observations. In case of *Fish*, the
 398 simulations also fall short in representing a comparable area fraction, albeit less markedly
 399 deficient than for the case of *Flowers*. Among all the patterns, *Gravel* best matches the
 400 observations.

401 While most patterns do not show a strong dependence on resolution at the sim-
 402 ulated scales, and might even slightly degrade like *Sugar*, *Gravel* improves its match with
 403 the observed area-fraction, Fig. 9. The bias in the fractional coverage of *Gravel* relative
 404 to the observations reduces from 35% to 13%. In the coarser ICON-624m run some *Flow-*
 405 *ers* patches were identified, but remained largely unrepresented independent of their ob-

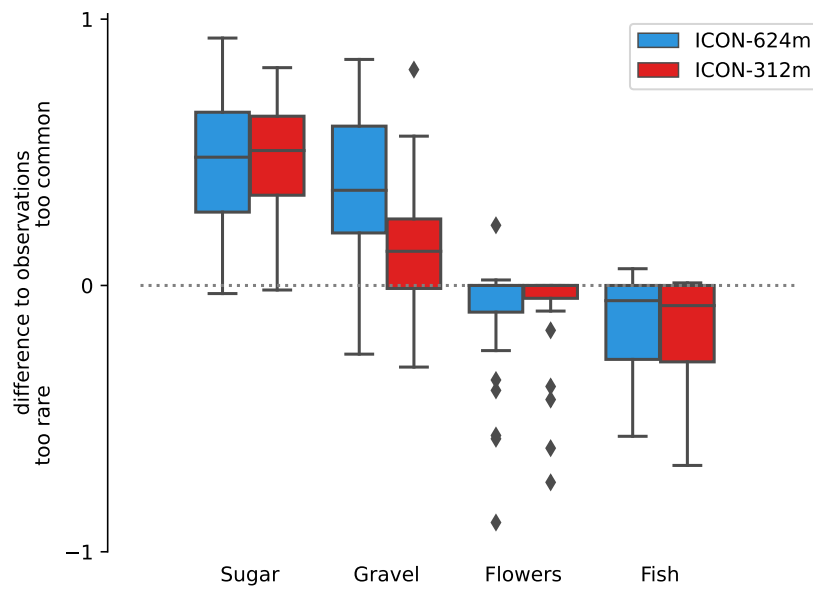


Figure 9. Difference in area-fraction occupied by patterns as identified by the neural network in the model simulations and observations. Boxes indicate the interquartile range around the median value. Whiskers extend this range by an additional 1.5 times the interquartile range. Outliers outside of the whiskers are marked with diamonds.

406 served area fraction. It should be noted that during the EUREC⁴A campaign *Flowers*
 407 mostly consisted only of a few clusters, causing the mean area fraction of *Flowers* to be
 408 close to zero with only a few outlier representing larger clusters (Fig.9).

409 3.3 Cloudiness

410 3.3.1 Cloud cover

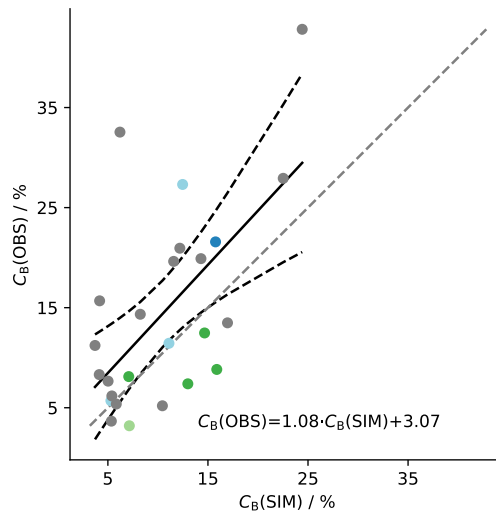


Figure 10. Daily cloud cover as derived from GOES-16 ABI and its simulated counterpart in ICON-312m for days without high cloud cover. Colored markers indicate dominant meso-scale cloud patterns as detected in satellite observations. The identity line is dashed in grey. Linear fit is shown together with the 95%-confidence interval in black.

411 A basic motivation for studying trade-wind clouds is to better understand what
 412 controls different measures of cloud amount, both in the mean and its variability. As dis-
 413 cussed above, and in the other previously cited studies, cloud cover is one of the most
 414 distinguishing factors across the different meso-scale patterns. It is this aspect of the pat-
 415 terns that makes them interesting to study. In this section we explore how well the sim-
 416 ulations represent the mean cloud cover, its vertical profile, its synoptic and diurnal vari-
 417 ability, and how this varies with environmental changes accompanying the emergence of
 418 different patterns in the observations. The radiative signature of clouds is discussed in
 419 § 3.6.

420 To compare the cloud cover of the simulations with satellite observations, we rely
 421 again on the brightness temperatures of measured and simulated satellite images. Sim-
 422 ilar to Bony et al. (2020) we define shallow clouds by a brightness temperature between
 423 270 K and 290 K, and denote by C_B the fraction of the domain covered by such clouds.
 424 Clouds with a colder brightness temperature are excluded from the calculation, as well
 425 as areas which are in close proximity to colder temperatures to account for thin cirrus
 426 clouds that can otherwise be misclassified as low-clouds.

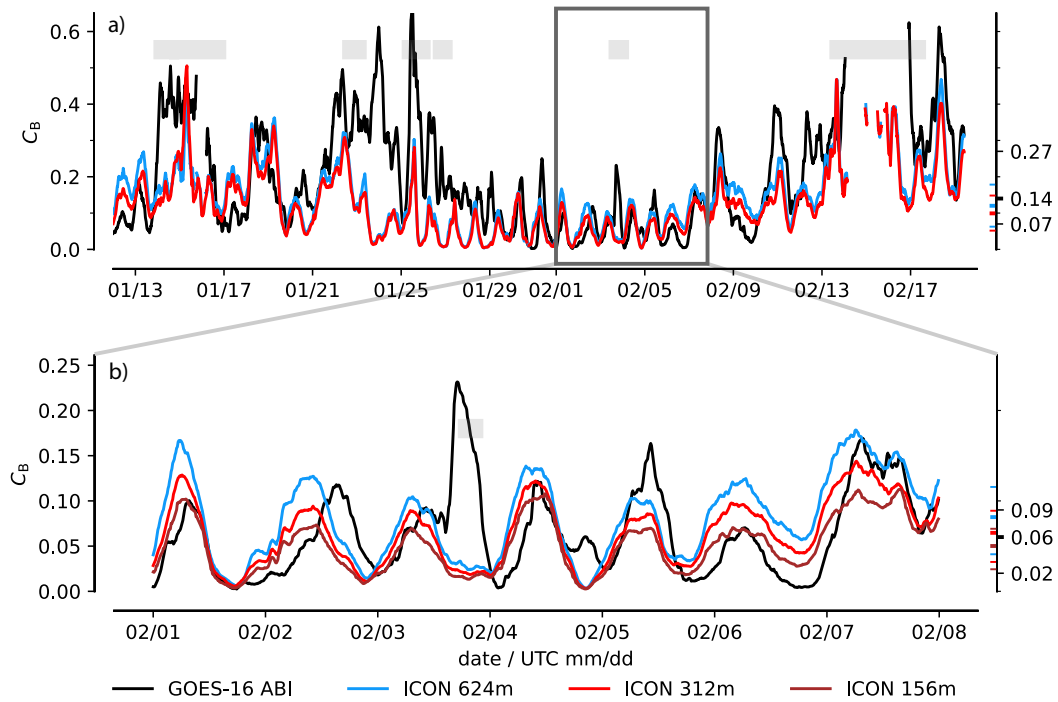


Figure 11. Timeseries of cloud cover (C_B) inferred from actual and synthetic satellite images for the entire analysis period (a). (b) magnifies the time period February 1 to February 7 and includes the result of ICON-156m. Periods that include more than 10% of high clouds based on brightness temperature being below 270 K are indicated by gray bars in (a,b). Missing low-cloud fractions indicate the presence of high clouds of 50% or more. The median and 25th/75th percentile are indicated by thick/thin labeled major ticks on the left y-axis excluding periods with high clouds.

427 Day-to-day variability in C_B agrees well with what was observed by GOES-16 ABI,
 428 Fig. 10. The simulated cloud cover is biased slightly low compared to the observations,

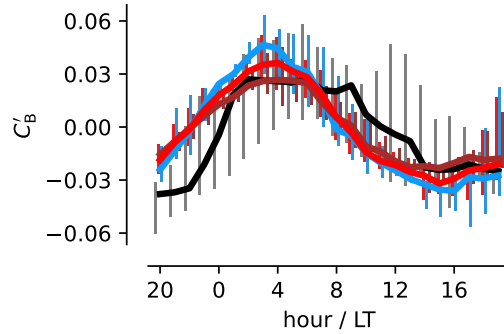


Figure 12. Median diurnal cycle as anomaly to the daily mean within the time-period shown in Fig. 11c without contributions from high-clouds.

429 but changes in the simulated daily cloud-cover vary almost one-to-one (on average) with
 430 the observations.

431 Although the simulations appear to capture variations in day-to-day cloud cover
 432 on average, there is considerable variability, and there are days where the observed C_B
 433 are in the upper quantile of its distribution, while the simulated C_B is in its lower quan-
 434 tile. Discrepancies are most apparent in the time-series, e.g. between January 21 and
 435 January 27, during the presence of high clouds and large cloud decks. Cases where more
 436 than 10% of the domain contain brightness temperatures below 270 K are marked with
 437 a gray horizontal bar in Fig. 11. Fig. 11, however, also highlights that a factor of two
 438 discrepancy in cloud amounts can appear on days without high-clouds, for instance on
 439 6 Feb. 2020, which has been classified as dominated by *Sugar* in the observations.

440 The simulations appear to roughly capture both the variability of C_B across days,
 441 as it varies with synoptic conditions, and variability within a day. To better quantify the
 442 simulation of the diurnal cycle of C_B without the contributions of high clouds we focus
 443 on the 1-7 Feb period, with the exclusion of Feb 3. The ICON-156m output available
 444 during this period helps to investigate any resolution sensitivity. The time-series of C_B
 445 over this period is presented in Fig. 11b, and as a composite in Fig. 12. The mean C_B
 446 over this period is observed to be 5.6% (GOES-16 ABI) and 8.2%, 6.5%, and 5.0% for
 447 ICON-624m, ICON-312m, and ICON-156m respectively. However, this improvement with
 448 resolution holds only true on average for this time-period. Across all days without high-
 449 clouds during the simulated period the observed cloud cover is 13.5%, while the model
 450 simulates 12.0% (ICON-624m) and 9.9% (ICON-312m). Because the cloudiness reduces

451 systematically with increasing resolution, the bias to the observations on a day-by-day
 452 basis varies and does not always improve. The coarser resolution run achieves particu-
 453 larly better agreement with the observations when stratiform clouds are observed. Pre-
 454 vious work which shows a sensitivity to grid aspect ratio (Kazil et al., 2021, Stevens et
 455 al., 2001, 1999) emphasizes how for many of these quantities the resolution remains marginal
 456 or even insufficient to provide precise quantitative estimates.

457 The amplitude of the observed diurnal cycle is 6%, and 9%, 7% and 6% for ICON-
 458 624m, ICON-312m and ICON-156m, respectively. The simulations show a clearer max-
 459 imum in cloudiness at about 04 LT, which decreases through the morning and into the
 460 early afternoon. In contrast, the observations show cloudiness to decrease slower through-
 461 out the morning hours (Fig. 12). This is attributable to the stratiform cloud amount on
 462 Feb 2 and Feb 4 that develops in the observations and that is not sufficiently represented
 463 by the simulations. Excluding these days from Fig. 12 reduces the discrepancies in the
 464 morning hours (not shown). Qualitatively our results agree with Vial et al. (2019) but
 465 show an overall lower amplitude in the diurnal cycle. Besides different definitions of cloudi-
 466 ness, the simulated time-period of the NARVAL campaign was particularly cloudy (Vial
 467 et al., 2019).

468 **3.3.2 Vertical cloud distribution**

469 The vertical distribution of cloudiness is important for structuring the cloud albedo,
 470 but also for the development of cloud microphysical processes. In addition to assessing
 471 how well this is represented across the EUREC⁴A period we also explore how it varies
 472 as a function of the observed meso-scale pattern of cloudiness, as Schulz et al. (2021) doc-
 473 umented systematic variations in the vertical structure of cloudiness across patterns.

474 For this purpose we examine the vertical distribution of cloudiness by means of the
 475 high-frequency (60 s) ICON-LEM column output (meteogram) at the location of the BCO.
 476 Because the definition of cloudiness is sensitive to the measurement technique, we con-
 477 verted the output to reflectivity to facilitate comparison with the BCO radar data as de-
 478 scribed in Sec. 2.1.2 and adopt echo fraction $C_E(z)$ as our measure of cloudiness.

479 On average the simulated $C_E(z)$, shows a typical trade-wind profile (Fig. 13a) with
 480 a peak in cloudiness at the lifting condensation level at around 800 m and a slowly de-
 481 creasing cloudiness to the trade-inversion at about 2 km (Siebesma et al., 2003, Stevens

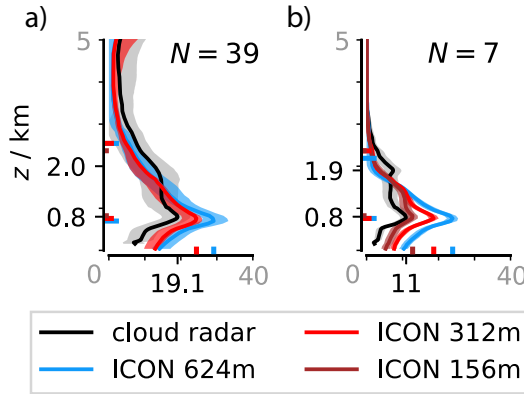


Figure 13. Cloud fraction variability for entire simulation period (a) and for the subsection of Feb 1 to Feb 7 when ICON-156m was also active (b). Standard error is shaded. Labeled ticks mark height and extent of maximum cloud fraction and height of the inversion based on the radar observations in former and soundings from Stephan et al. (2021) in the later. Colored ticks indicate the identical values for the simulations. The inversion height is defined as the height of the maximum vertical gradient of the liquid water potential temperature (θ_l).

482 et al., 2001). The simulations show a tendency toward a more bottom heavy profile of
 483 cloudiness, with an overestimate that is largest near the LCL and through the sub-cloud
 484 layer. This difference reduces with resolution, from 10 % (ICON-624m) to 5 % (ICON-312m).
 485 For the 1-7 Feb period, the differences are also apparent, but less so for the ICON-156m
 486 simulation (2 %) (Fig. 13b). These biases extend to the near surface echo fraction, which
 487 suggests that they are associated with precipitation. The better correspondence to the
 488 observations with improved resolution is apparent at all levels, also in the near-surface
 489 echo fractions, and is consistent with earlier studies of more idealized cases (Stevens, Ac-
 490 quistapace, et al., 2020).

491 Compositing $C_E(z)$ over days associated with observations of particular meso-scale
 492 pattern allows us to test the pattern dependent skill of the simulations. Here, a day with
 493 a meso-scale pattern is defined as the prevailing pattern type manually identified in the
 494 C³ONTEXT dataset at the location of the Barbados Cloud Observatory. The separa-
 495 tion reveals that the differences between simulations and observations do depend on the
 496 observed meso-scale context. The best resembled profile of $C_E(z)$ is the one of *Gravel*.
 497 The cloudiness at the lifting condensation level is well matched, especially for the higher
 498 resolution run. Further aloft it follows closely the observed distribution. For *Gravel* the

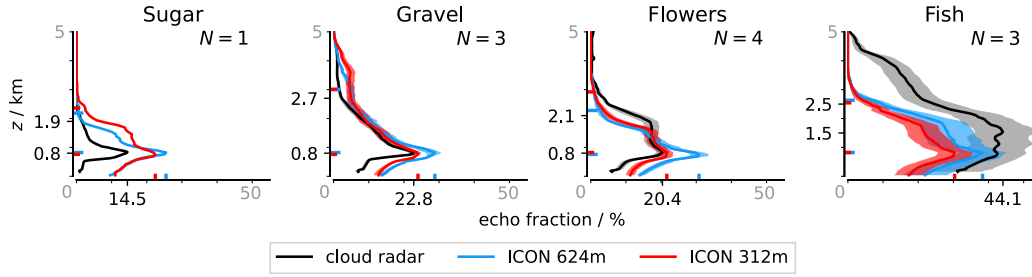


Figure 14. As Fig. 13a but here for days where meso-scale patterns were identified in the observations following Schulz (2022). N defines the number of days found for each group.

499 main discrepancies are below the lifting condensation level, where the echo fraction in-
 500 dicates more precipitation.

501 The simulations overestimate the near-surface echo fraction (which we associate
 502 with rain or drizzle) not only for *Gravel*, but also for *Sugar*, *Flowers* and the overall av-
 503 erage as well. The underestimation of rain frequency in case of *Fish*, along with its gen-
 504 erally lower vertical extent, hint to a reduced activity of the remaining frontal system
 505 that is thought to structure the *Fish* patterns (Schulz et al., 2021). This analysis also
 506 points out how the simulations are limited by sample size for large-scale patterns such
 507 as *Fish*. Only one *Fish* passed the Barbados Cloud Observatory, albeit over three days
 508 between January 21 and January 23. Given the point-wise comparison, co-location bi-
 509 ases make it difficult to establish the source of differences between the observed and sim-
 510 ulated profiles. The supplemental movie shows that this *Fish* pattern was well developed
 511 and passed over the observatory also in the simulations². However, it also reveals that
 512 in the simulations the pattern developed stronger in the east and decayed earlier in the
 513 west where the BCO is located. This development explains the shallower and more sup-
 514 pressed convection that resembles *Sugar* on January 24th and the reduced occurrence
 515 of deeper (3 km to 4 km) clouds in the mean. The difference in cloud fraction in Fig. 11
 516 reflects this.

517 The issue of representing the cloud fraction at the base of the trade-wind inversion,
 518 z_i , becomes again apparent and especially visible in the case of *Flowers*. $C_E(z_i)$ is par-
 519 ticularly underestimated. The differentiation of the echo fraction profile across patterns

² <https://www.doi.org/10.5281/zenodo.7567204>

520 is less strong in the simulations as observed. *Sugar* and *Flowers* profiles are alike in the
 521 simulations, while *Sugar* is distinguishable from *Flowers* in the observations by the lack
 522 of deeper clouds and a vanishing amount of $C_E(z = 0\text{ m})$.

523 3.4 Precipitation

524 While the above sections have shown that the echo fraction below cloud base and
 525 therefore the rain frequency is too high on average, their daily anomalies agree reason-
 526 ably well. (Fig. 15). Both observed and simulated anomalies approach 30%. The out-
 527 liers seen in Fig. 15 in the lower right quadrant are for January 18 and January 19, when
 528 the clouds were organized by a large-scale system that developed a strong large-scale con-
 529 trast in cloudiness with the Barbados Cloud Observatory residing mostly in the clear-
 530 sky area. In the simulation the organization was less strong and positioned closer to the
 531 location of the Barbados Cloud Observatory leading to the large offset. The opposite is
 532 true for January 23 during the passage of the *Fish* pattern, when the pattern passed the
 533 BCO closer in reality (upper left quadrant).

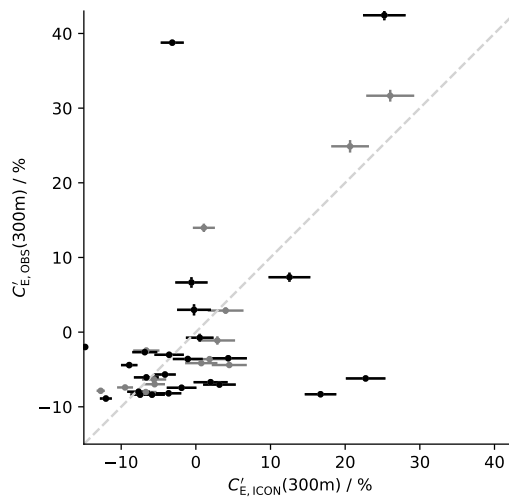


Figure 15. Echo fraction at 300 m ASL at the Barbados Cloud Observatory location is representative of the rain fraction. Daily anomalies of rain fraction to the entire time series are plotted for radar observations and the ICON-312m simulation. Standard error is calculated based on rolling windows of four hours and indicated as daily average. Grey dashed line indicates the one-to-one line. Grey markers represent days with high clouds.

534 The distribution of echo intensities contributing to the echo fraction differ more sub-
 535 stantially between the observations and simulations. This is shown in Fig. 16 which com-
 536 pares the echo intensity distribution at three heights. Below cloud base the observed echo
 537 intensities are more uniformly distributed, with echos between -50 dBZ to -25 dBZ be-
 538 ing found as often as echoes between -25 dBZ to 0 dBZ. In the simulations it is rather
 539 rare to sample echos less than -25 dBZ, which is compensated by echos around -15 dBZ
 540 being twice as frequent as observed. Also stronger echos, indicative of more intense rain,
 541 are much less likely in the simulations, although differences are exaggerated by the sat-
 542 uration of the near-surface radar return at about 15 dBZ. Near cloud base the observa-
 543 tions also show the emergence of a second mode, with the frequency of echos increasing
 544 as the reflectivity decreases below -25 dBZ. The opposite behavior in the simulations
 545 likely highlights the inability of the simulations to represent the deliquescence of large
 546 cloud condensation nuclei, which were shown by Klingebiel et al. (2019) to be quite com-
 547 mon at the BCO. At 1500 m where echos are expected to reflect the onset of more ac-
 548 tive coalescence of the lofted hydrometeors, rather than a mixture of precipitation from
 549 above with the in-situ microphysical development of aerosol and cloud droplets, the match
 550 between the simulations and observations is better, albeit perhaps less variable in the
 551 simulations. The poorness of fit is not sensitive to how we look at the data, as using wider
 552 bins in the pdf, or using a cumulative distribution function (not shown) leads to simi-
 553 lar conclusions. The reflectivities might be a useful blueprint on how microphysical pro-
 554 cesses are represented in LES, and thus provide a test of microphysical models.

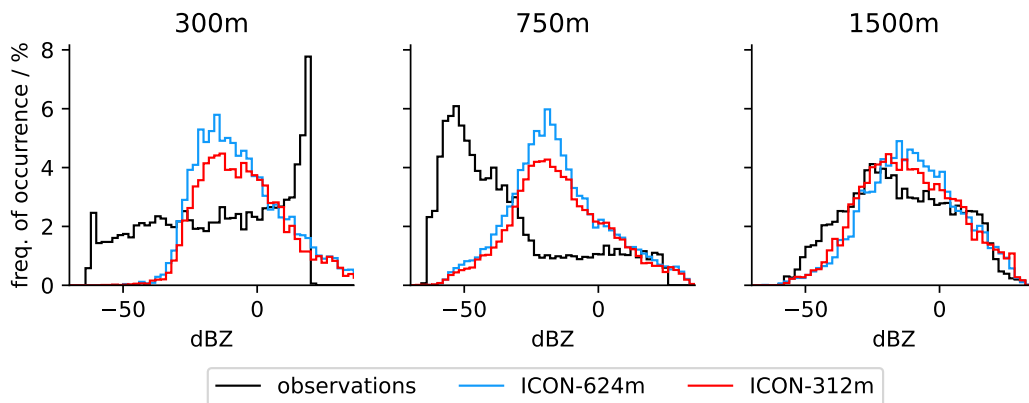


Figure 16. Reflectivity histograms based on radar observations at the BCO and their syn-
 thetic counter-part for the simulations within the subcloud-layer (300 m), around the cloud base
 height (750 m) and above (1500 m).

555

3.5 Environmental influence on cloud fraction

556

557

558

559

560

561

562

563

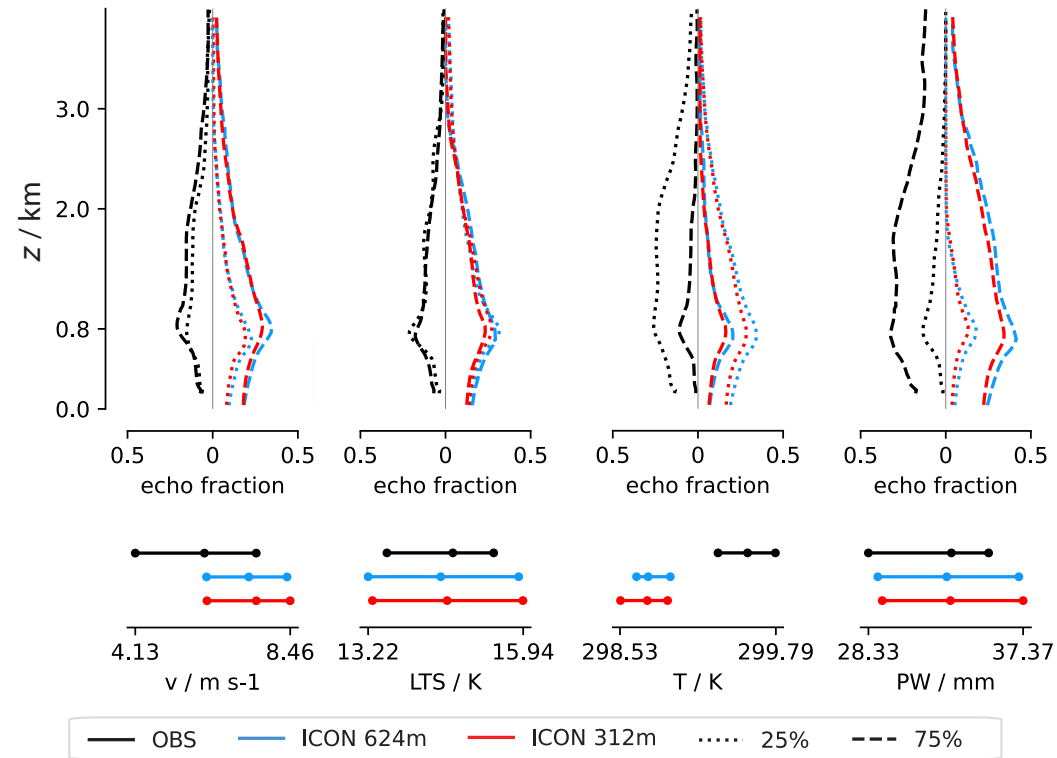


Figure 17. Dependence of echo fraction on daily averaged environmental conditions (left to right: 10m wind speed, 2m-temperature, lower tropospheric stability and precipitable water) in both observations (black profiles) and simulations (colored profiles). The 25th-75th percentile range and median of environmental conditions are shown in the lower panel. Dotted (dashed) profiles correspond to the lower (upper) 25th percentile of environmental conditions. Observations: black; ICON-624m: red; ICON-312m: orange.

564 Fig. 17 illustrates how $C_E(z)$ varies with the three most common environmental
 565 conditions correlating with meso-scale variability, wind-speed, temperature and inver-
 566 sion strength, as identified by Bony et al. (2020) for both observations and simulations.
 567 In addition, we also explore co-variability of $C_E(z)$ and precipitable water (PW), as Nui-
 568 jens et al. (2009) identified this as a controlling factor. Despite differences in the distri-
 569 bution of environmental factors (Fig. 17), the near mirror symmetry between the ob-
 570 served profile of the 25th and 75th percentiles of $C_E(z)$ and those simulated, measures
 571 the similarity between the two, something which is relatively independent of resolution.
 572 Temperature and precipitable water separates the cloud-fraction profiles best compared
 573 to LTS and wind speed. The sensitivity to precipitable water was also seen (in their case
 574 for θ_e) in the analysis of trade-wind clouds during RICO (Nuijens et al., 2009). While
 575 the simulations lack cloudiness around 2km in the low temperature case, and to some
 576 extent at low wind-speeds, the shallower clouds in the warm case are well resembled. No-
 577 tably, the precipitation change is captured well when comparing the echo fractions of the
 578 lowest levels, but is generally too strong.

579 Although wind-speed has been identified to distinguish well between the different
 580 meso-scale patterns (Bony et al., 2020, Schulz et al., 2021) it mostly acts along patterns
 581 of similar cloud fractions (see Fig. 3 of Bony et al. (2020)) and separates *Gravel* from
 582 *Sugar* and *Fish* from *Flowers*. The similar profiles for both wind-speed quantiles in the
 583 observations is consistent with such behavior. The simulations show more of a differen-
 584 tiation, something also seen in the analysis by Nuijens et al. (2009) across the lower and
 585 middle terciles in cloudiness. Based on the analysis of meso-scale patterns of variabil-
 586 ity we would expect a greater differentiation among quantiles for the LTS, this is how-
 587 ever not evident in either the observations or simulations, similar to what was found by
 588 Nuijens et al. (2009) and perhaps indicative of a lack of *Flowers* in both that and the
 589 present study.

590 3.6 Radiative effects

591 In this section we return to the question of cloud cover, as seen through the effect
 592 of clouds on the irradiances at the top of the atmosphere. These are, after all, the ef-
 593 fects that underpin our interests in trade-wind clouds in the first place, and the patterns
 594 of cloudiness which are shown to modulate them.

595 Here we use the Clouds and the Earth’s Radiant Energy System (CERES) Syn-
596 optic (SYN) 1 degree (SYN1deg) product which is enhanced with geostationary satel-
597 lite data to capture the diurnal cycle (NASA/LARC/SD/ASDC, 2017). This introduces
598 a potential bias as the interpretation of the geostationary data is based on modelling,
599 whose fidelity on a day-to-day basis has (to our knowledge) not been investigated but
600 is of importance when capturing the cloudiness of meso-scale cloud pattern in the trades
601 (Vial et al., 2021). In addition, the model top-of-the-atmosphere (TOA) is at 21 km caus-
602 ing slight differences in the absolute TOA fluxes.

603 Overall the simulations reasonably represent the day-to-day variability in the top-
604 of-atmosphere irradiances. Fig. 18(a) shows how well the simulated top-of-atmosphere
605 outgoing irradiances matches observations. The distribution is well balanced along the
606 identity line, more so when cases with high-clouds are excluded. There is a net bias of
607 about 5.5 W m^{-2} , with the simulations cooling less than observed. In both the obser-
608 vations and the simulations, *Flowers* with their large stratiform layers (at least in the
609 observations) and dry free-troposphere are associated with days that radiate more heat
610 to space in the net as compared to *Gravel* days which are close to a net zero at the top
611 of the atmosphere.

612 Simulated cloud radiative effects agree less well with the observations in particu-
613 lar in the day-to-day variability. Discrepancies between cloud top temperature, liquid
614 water content and organization of clouds impact both the cloudy fluxes as well as the
615 clearsky fluxes. While the latter co-vary well with the observations (Fig.S4) and are mostly
616 influenced by the amount of daylight hours, while remaining a constant albedo, they can-
617 not explain the variability in the shortwave cloud radiative effect of up to $\pm 100\%$. The
618 variability of the longwave cloud radiative effect is much smaller, in particular in the sim-
619 ulations and shows very little relationship to the observed one (Fig.18c). The day-to-
620 day variability in net cloud radiative effect is therefor mainly driven by the shortwave
621 cloud radiative effect (Fig. 18b), but correlation between the observations and simula-
622 tions remain weak and substantially less than that for the cloud amount. While our sus-
623 picion is that most of the biases arise from deficiencies in the simulations and slightly
624 different developments of the dynamics affecting particularly the *Fish* pattern, given the
625 way in which CERES must infer the diurnal cycle using angular distribution models, which
626 may not be optimized for shallow clouds, it is also not immediately obvious to what ex-
627 tent the measurements are free of random errors.

628 As to be expected the net cloud radiative effect, is dominated by the short-wave
629 component, but due to the deleterious effect of the long-wave cloud radiative effects, its
630 simulated value correlates even less well with the observations. This analysis, underlines
631 the difficulty of quantitatively simulating cloudiness, even with relatively fine mesh and
632 large domain simulations, perhaps not something that is unexpected given the sensitiv-
633 ity of idealized simulations to the implementation (numerics) (Stevens et al., 2001), as-
634 sumptions that remain in parameterized processes and the simulation setup (vertical res-
635 olution, aspect ratio) (Kazil et al., 2021) in general.

636 4 Conclusion

637 The ability of the ICON large-eddy model to quantitatively capture the thermo-
638 dynamic structure of the trade-wind boundary layer, and the clouds that form within
639 it, has been evaluated using data collected from the EUREC⁴A field study.

640 Simulations were performed using the ICON model for 41 days from 9 January through
641 19 February 2020, over exceptionally large domains spanning the trade-wind domain and
642 time period of EUREC⁴A. Simulations were performed using multiple nests, with grid
643 spacings of 312 m and 624 m, and with a yet finer inner nest for an additional seven day
644 period between 1 and 7 February. Their large spatial and temporal extent of more than
645 1000 km in the zonal direction and 500 km in the meridional direction at the hm-scale
646 resolution expands our view on trade-wind variability.

647 The simulation strategy, whose large domains enable the simulations to capture the
648 scale at which trade-wind clouds organize, combined with the measurement strategy that
649 statistically sampled the boundary layer over a large meso-scale region, provides a ba-
650 sis for quantifying the ability of coarse grid large-eddy simulations to represent the trade-
651 wind boundary layer and trade-wind clouds, something that, until now, has only been
652 done for limited temporal and/or spatial extents. Here, a united view on individual cases
653 and processes studied in the past is presented by including BOMEX- and RICO-like con-
654 vection that naturally occur within the simulated variability. The evaluation is further
655 aided through the use of the forward operators RTTOV and PAMTRA to allow for a
656 more quantitative comparison to both satellite imagers and surface-based cloud radars.
657 The satellite simulator (RTTOV) also enabled the use of a neural-network based pat-
658 tern classification scheme trained on labeled observations.

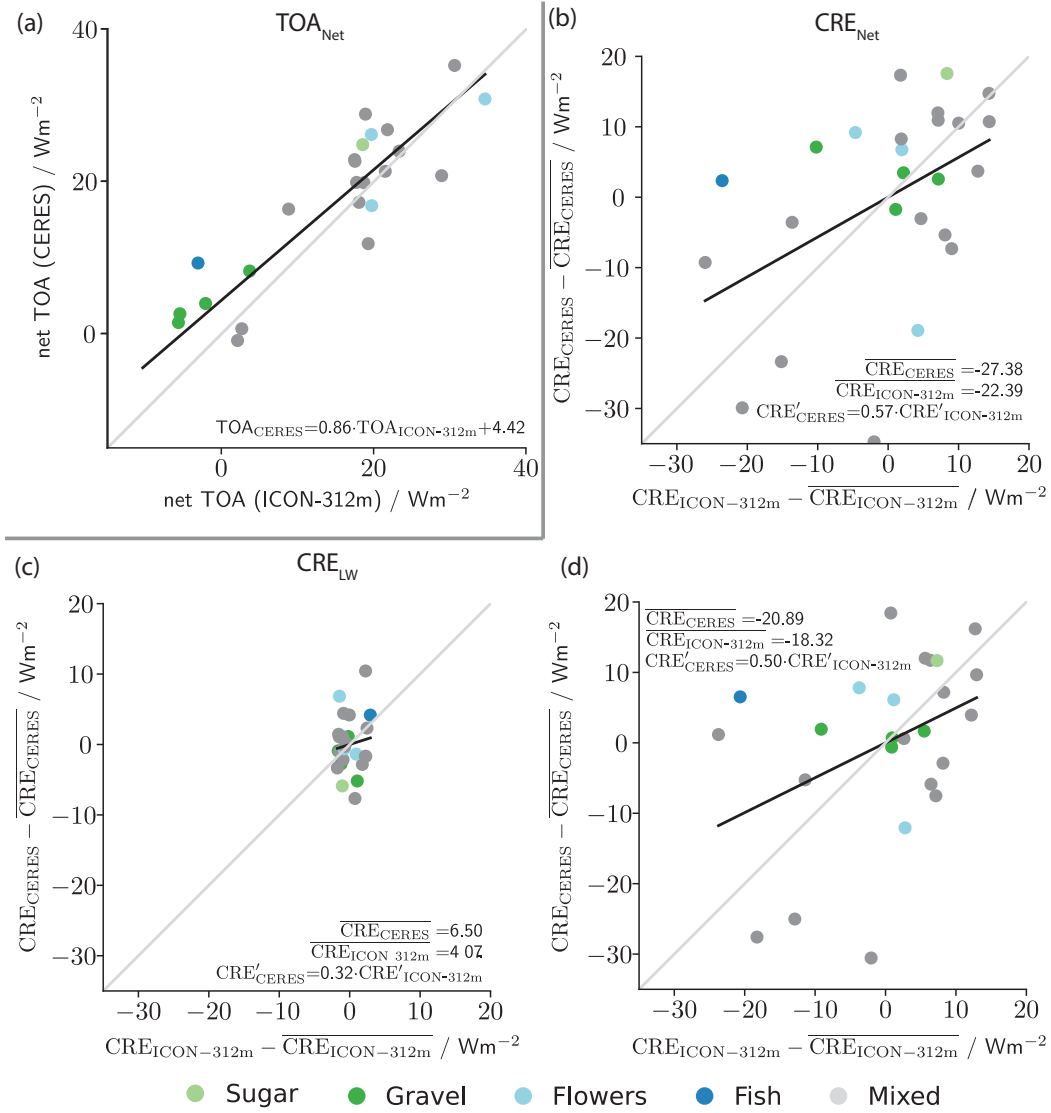


Figure 18. (a) Net TOA fluxes of ICON-312m and CERES. (b,c,d) Daily anomaly of cloud radiative effect relative to the studied time-series average (faint markers: entire time-series; bold markers: days with low clouds only). Colored markers indicate dominant meso-scale cloud patterns as detected in satellite observations.

659 The simulations are shown to reasonably represent the mean structure of the trade-
 660 wind boundary layer, as measured by the profile of winds, clouds, and thermodynamic
 661 variables measured during EUREC⁴A. The match is not perfect, with the simulated bound-
 662 ary layer being cooler (1 K) and drier (1 g kg^{-1}) than the observed boundary layer, for
 663 reasons that may partly be due to a 0.4 K to 0.6 K under-estimate of the sea-surface tem-
 664 peratures by the reanalysis. The simulated boundary layer also shows less differentia-

665 tion between the cloud and inversion layer than is observed, also in the mean. The spa-
666 tial distribution of cloudiness, in particular its match with the observed arrangement,
667 have been quantified by the detectability of the neural network. The simulations are able
668 to capture differences in the meso-scale structure underlying different meso-scale pat-
669 terns of cloudiness, but have difficulty in fully representing the cloud-forms that accom-
670 pany these patterns (Schulz et al., 2021). In particular there is a deficit of stratiform clouds
671 in association with the *Flowers* pattern, following the taxonomy of Stevens, Bony, et al.
672 (2020), and *Sugar* is more wide-spread than observed.

673 The observed coverage of low-clouds, of about 14%, is well captured by the sim-
674 ulations, ironically somewhat more so on the coarser grids, as cloud cover progressively
675 decreases from 12.0% to 9.9% for the 624 m and 312 m simulations respectively, suggest-
676 ing that the goodness of fit at coarser resolution may benefit from compensating errors
677 which depend differently on the horizontal versus the vertical grid-spacing. The simu-
678 lations also well represent day-to-day variability in cloudiness, and the mean diurnal cy-
679 cle – whose amplitude is about 6 %, or half of the mean – increasingly so as resolution
680 is refined.

681 The vertical distribution of cloudiness, as measured by the echo fraction at the Bar-
682 bados Cloud Observatory and compared to a vertically pointing cloud radar at that site,
683 agrees reasonably well with the observations. The simulated cloud fractions maximize
684 near cloud base, at about 800 m, and decay over a roughly 2 km cloud layer. The sim-
685 ulations tend to slightly over-estimate cloud base cloudiness and under-estimate cloudi-
686 ness near the base of the trade inversion, with again too little differentiation between the
687 cloud and inversion layers. The vertical structure of cloudiness improves markedly with
688 the refinement of horizontal resolution, but even at 156 m grid spacing the inversion layer
689 and its clouds are still poorly differentiated from the cloud layer. Compositing across canon-
690 ical patterns of mesoscale organization highlight the challenge the simulations have in
691 representing *Sugar*. While prevalent in the simulations, simulated *Sugar* is character-
692 ized by cloud-base cloud fractions that are a factor of two too large, and simulated *Flow-*
693 *ers* days show little sign of enhanced stratiform cloudiness. All in all, the simulations
694 mainly differentiate *Sugar* from *Flowers* from *Gravel* by progressively deepening the cloud
695 layer, but not otherwise changing the vertical distribution of echo fraction, in marked
696 contrast to the observations. Despite the difficulty in differentiating among meso-scale
697 cloud patterns, the simulations show cloudiness varying with environmental conditions

698 in ways that mimic the data, with precipitable water, near surface temperatures and wind
699 speeds most clearly influencing cloud amount.

700 The simulations tend to over-estimate the echo fractions in the sub-cloud layer, in-
701 dicative of too much, perhaps too light, precipitation. They also represent a much nar-
702 rower distribution of echo intensities at cloud base and in the sub-cloud layer than is seen
703 in the radar data. The day-to-day variability, i.e., the variation in precipitation with syn-
704 optic conditions, appears to be reasonably well captured, as is the reflectivity distribu-
705 tion within the cloud layer.

706 Although the simulated average cloud cover and the net TOA radiation match well
707 with the observations, the day-to-day anomalies in cloud radiative effects as measured
708 by CERES prove difficult to reproduce. Day-to-day variability in long-wave cloud radia-
709 tive effects is uncorrelated, or perhaps even negatively correlated with the observations,
710 and short-wave cloud radiative effects are only weakly correlated with the data. Differ-
711 ences in clearsky radiation can explain some of the offset in CRE, but are rather con-
712 stant and cannot explain day-to-day discrepancies (see Fig.S4). The cause for the poor
713 match between observed and simulated cloud radiative effects merits further investiga-
714 tion, also with possible limitations in the data in mind.

715 For investigating these effects, but also other biases such as the overly cool and dry
716 boundary layer, and the difficulty in developing a stratiform cloud layer, we show that
717 the seven day period between 1-7 February may suffice. This period is particularly use-
718 ful for a more in-depth study as it encompasses two periods of *Flowers* and one of *Sugar*,
719 which presents some of the greatest challenges for the simulation: (1) the too frequent
720 and invariable precipitation produced by the microphysical parameterization, (2) the lack
721 of convergence of cloud amount at the lifting condensation level with increasing resolu-
722 tion, (3) the representation of stratiform cloud amount, and ultimately (4) the meso-scale
723 differentiation of *Flowers* and *Sugar*. Past experience suggests that using less diffusive
724 numerical methods can favor the development of stratiform clouds (e.g. Stevens et al.
725 (2001)), but often also in situations like for *Sugar*, when they do not form. Hence, sim-
726 ulating both with quantitative fidelity poses a critical test for hecto-meter scale simu-
727 lations and the turbulence and microphysical models that accompany them.

728 EUREC⁴A measured a wealth of data, only a small amount of which is used here.
729 For instance additional cloud radar data is available from research vessels and research

730 aircrafts, as is water vapor profiling, and passive microwave measurements capable of con-
731 straining cloud water. The synergy of large-domain large-eddy simulations and the EUREC⁴A
732 observations will help to connect individual measurements and create the bigger picture
733 of the dynamics driving the observed meso-scale organization. Here, we have demonstrated
734 that LES are capable to form patterns of meso-scale organization, but that challenges
735 to quantitatively represent the observed structure of the ensuing boundary layer clouds
736 remain.

737 **5 Open Research**

738 The simulation output and observations from the EUREC⁴A campaign are freely
739 available and can be easily accessed via the EUREC⁴A-Intake catalog at [https://github](https://github.com/eurec4a/eurec4a-intake)
740 [.com/eurec4a/eurec4a-intake](https://github.com/eurec4a/eurec4a-intake) as described at howto.eurec4a.eu. The processing scripts
741 are available at doi.org/10.5281/zenodo.7591545. GOES-16 Advanced Baseline Im-
742 ager Level 1b radiances are available at doi.org/10.7289/V5BV7DSR and were converted
743 with Raspaud et al. (2019) to brightness temperatures. MODIS imagery originates from
744 the NASA Worldview application (<https://worldview.earthdata.nasa.gov>), part of
745 the NASA Earth Observing System Data and Information System (EOSDIS). The ERA5
746 output used in this study (Hersbach, H. et al., 2018) has been provided by the Climate
747 Data Store. The Clouds and the Earth’s Radiant Energy System (CERES) product used
748 is available at NASA/LARC/SD/ASDC (2017)

749 **6 Acknowledgement**

750 The authors are grateful to the members of the Tropical Cloud Observation group
751 for maintaining the Barbados Cloud Observatory and continuously increasing its valu-
752 able data-set. The authors thank Daniel Klocke for conducting the ICON-SRM simu-
753 lations and his valuable comments regarding ICON in general. Robert Vicari is thanked
754 for implementing an updated version of the satellite forward operator interface into ICON.
755 This work used resources of the Deutsches Klimarechenzentrum (DKRZ) and the authors
756 are thankful for the granted compute time and storage. Three anonymous reviewers are
757 thanked for their valuable feedback that improved our manuscript. We appreciate Tapio
758 Schneider’s comments and editorial handling.

759 **References**

- 760 Albright, A. L., Bony, S., Stevens, B., & Vogel, R. (2022, September). Observed
 761 Subcloud-Layer Moisture and Heat Budgets in the Trades. *Journal of the Atmo-*
 762 *spheric Sciences*, *79*(9), 2363–2385. doi: 10.1175/JAS-D-21-0337.1
- 763 Atlas, R. L., Bretherton, C. S., Blossey, P. N., Gettelman, A., Bardeen, C., Lin, P.,
 764 & Ming, Y. (2020). How Well Do Large-Eddy Simulations and Global Climate
 765 Models Represent Observed Boundary Layer Structures and Low Clouds Over the
 766 Summertime Southern Ocean? *Journal of Advances in Modeling Earth Systems*,
 767 *12*(11), e2020MS002205. doi: 10.1029/2020MS002205
- 768 Baldauf, M., Seifert, A., Förstner, J., Majewski, D., Raschendorfer, M., & Rein-
 769 hardt, T. (2011, December). Operational Convective-Scale Numerical Weather
 770 Prediction with the COSMO Model: Description and Sensitivities. *Monthly*
 771 *Weather Review*, *139*(12), 3887–3905. doi: 10.1175/MWR-D-10-05013.1
- 772 Bony, S., & Dufresne, J.-L. (2005). Marine boundary layer clouds at the heart of
 773 tropical cloud feedback uncertainties in climate models. *Geophysical Research Let-*
 774 *ters*, *32*(20), n/a–n/a. doi: 10.1029/2005GL023851
- 775 Bony, S., Schulz, H., Vial, J., & Stevens, B. (2020). Sugar, Gravel, Fish, and
 776 Flowers: Dependence of Mesoscale Patterns of Trade-Wind Clouds on Environ-
 777 mental Conditions. *Geophysical Research Letters*, *47*(7), e2019GL085988. doi:
 778 10.1029/2019GL085988
- 779 Bony, S., & Stevens, B. (2019, March). Measuring Area-Averaged Vertical Motions
 780 with Dropsondes. *Journal of the Atmospheric Sciences*, *76*(3), 767–783. doi: 10
 781 .1175/JAS-D-18-0141.1
- 782 Bony, S., Stevens, B., Ament, F., Bigorre, S., Chazette, P., Crewell, S., ... Wirth,
 783 M. (2017, September). EUREC4A: A Field Campaign to Elucidate the Cou-
 784 plings Between Clouds, Convection and Circulation. *Surveys in Geophysics*, *38*(6),
 785 1529–1568. doi: 10.1007/s10712-017-9428-0
- 786 Bretherton, C. S., & Blossey, P. N. (2017). Understanding Mesoscale Aggregation of
 787 Shallow Cumulus Convection Using Large-Eddy Simulation. *Journal of Advances*
 788 *in Modeling Earth Systems*, *9*(8), 2798–2821. doi: 10.1002/2017MS000981
- 789 Brient, F., Schneider, T., Tan, Z., Bony, S., Qu, X., & Hall, A. (2016, July). Shal-
 790 lowness of tropical low clouds as a predictor of climate models' response to warm-
 791 ing. *Clim Dyn*, *47*(1-2), 433–449. doi: 10.1007/s00382-015-2846-0

- 792 Dauhut, T., Couvreur, F., Bouniol, D., Beucher, F., Volkmer, L., Pörtge, V., ...
 793 Wirth, M. (2023). Flower trade-wind clouds are shallow mesoscale convective sys-
 794 tems. *Quarterly Journal of the Royal Meteorological Society*, 149(750), 325–347.
 795 doi: 10.1002/qj.4409
- 796 Dipankar, A., Stevens, B., Heinze, R., Moseley, C., Zängl, G., Giorgetta, M., &
 797 Brdar, S. (2015). Large eddy simulation using the general circulation model
 798 ICON. *Journal of Advances in Modeling Earth Systems*, 7(3), 963–986. doi:
 799 10.1002/2015MS000431
- 800 Gassmann, A. (2013). A global hexagonal C-grid non-hydrostatic dynamical core
 801 (ICON-IAP) designed for energetic consistency. *Quarterly Journal of the Royal*
 802 *Meteorological Society*, 139(670), 152–175. doi: 10.1002/qj.1960
- 803 George, G., Stevens, B., Bony, S., Pincus, R., Fairall, C., Schulz, H., ... Radtke, J.
 804 (2021, November). JOANNE: Joint dropsonde Observations of the Atmosphere
 805 in tropical North atlanTic meso-scale Environments. *Earth System Science Data*,
 806 13(11), 5253–5272. doi: 10.5194/essd-13-5253-2021
- 807 George, G., Stevens, B., Bony, S., Vogel, R., & Naumann, A. K. (2022, Septem-
 808 ber). *Ubiquity of shallow mesoscale circulations in the trades and their in-*
 809 *fluence on moisture variance.* Earth and Space Science Open Archive. doi:
 810 10.1002/essoar.10512427.1
- 811 Hartmann, D. L., Ockert-Bell, M. E., & Michelsen, M. L. (1992, November). The
 812 Effect of Cloud Type on Earth’s Energy Balance: Global Analysis. *Journal of Cli-*
 813 *mate*, 5(11), 1281–1304. doi: 10.1175/1520-0442(1992)005(1281:TEOCTO)2.0.CO;
 814 2
- 815 Heinze, R., Dipankar, A., Henken, C. C., Moseley, C., Sourdeval, O., Trömel, S., ...
 816 Quaas, J. (2017). Large-eddy simulations over Germany using ICON: A com-
 817 prehensive evaluation. *Quarterly Journal of the Royal Meteorological Society*,
 818 143(702), 69–100. doi: 10.1002/qj.2947
- 819 Hersbach, H., Bell, B., Berrisford, P., Biavati, G., Horányi, A., Muñoz Sabater,
 820 J., ... Thépaut, J-N. (2018). *ERA5 hourly data on single levels from 1979 to*
 821 *present.* Copernicus Climate Change Service (C3S) Climate Data Store (CDS).
 822 doi: 10.24381/cds.adbb2d47
- 823 Heus, T., & Seifert, A. (2013, August). Automated tracking of shallow cumulus
 824 clouds in large domain, long duration large eddy simulations. *Geosci. Model Dev.*,

- 825 6(4), 1261–1273. doi: 10.5194/gmd-6-1261-2013
- 826 Jacob, M., Kollias, P., Ament, F., Schemann, V., & Crewell, S. (2020, Novem-
 827 ber). Multilayer cloud conditions in trade wind shallow cumulus – confronting
 828 two ICON model derivatives with airborne observations. *Geoscientific Model
 829 Development*, 13(11), 5757–5777. doi: 10.5194/gmd-13-5757-2020
- 830 Kazil, J., Christensen, M. W., Abel, S. J., Yamaguchi, T., & Feingold, G. (2021).
 831 Realism of Lagrangian Large Eddy Simulations Driven by Renalysis Meteorol-
 832 ogy: Tracking a Pocket of Open Cells Under a Biomass Burning Aerosol Layer.
 833 *Journal of Advances in Modeling Earth Systems*, 13(12), e2021MS002664. doi:
 834 10.1029/2021MS002664
- 835 Klingebiel, M., Ghate, V. P., Naumann, A. K., Ditas, F., Pöhlker, M. L., Pöhlker,
 836 C., ... Stevens, B. (2019, February). Remote Sensing of Sea Salt Aerosol below
 837 Trade Wind Clouds. *Journal of the Atmospheric Sciences*, 76(5), 1189–1202. doi:
 838 10.1175/JAS-D-18-0139.1
- 839 Mech, M., Maahn, M., Kneifel, S., Ori, D., Orlandi, E., Kollias, P., ... Crewell,
 840 S. (2020, September). PAMTRA 1.0: The Passive and Active Microwave ra-
 841 diative TRAnsfer tool for simulating radiometer and radar measurements of the
 842 cloudy atmosphere. *Geoscientific Model Development*, 13(9), 4229–4251. doi:
 843 10.5194/gmd-13-4229-2020
- 844 Mlawer, E. J., Taubman, S. J., Brown, P. D., Iacono, M. J., & Clough, S. A. (1997,
 845 July). Radiative transfer for inhomogeneous atmospheres: RRTM, a validated
 846 correlated-k model for the longwave. *Journal of Geophysical Research: Atmo-
 847 spheres*, 102(D14), 16663–16682. doi: 10.1029/97JD00237
- 848 Narenpitak, P., Kazil, J., Yamaguchi, T., Quinn, P., & Feingold, G. (2021).
 849 From Sugar to Flowers: A Transition of Shallow Cumulus Organization Dur-
 850 ing ATOMIC. *Journal of Advances in Modeling Earth Systems*, 13(10),
 851 e2021MS002619. doi: 10.1029/2021MS002619
- 852 NASA/LARC/SD/ASDC. (2017, September). *CERES and GEO-Enhanced TOA,
 853 within-atmosphere and surface fluxes, clouds and aerosols 1-Hourly terra-aqua
 854 Edition* 4A. NASA Langley Atmospheric Science Data Center DAAC.
- 855 Nuijens, L., Medeiros, B., Sandu, I., & Ahlgrimm, M. (2015, June). The behavior
 856 of trade-wind cloudiness in observations and models: The major cloud compo-
 857 nents and their variability. *Journal of Advances in Modeling Earth Systems*, 7(2),

- 858 600–616. doi: 10.1002/2014MS000390
- 859 Nuijens, L., Serikov, I., Hirsch, L., Lonitz, K., & Stevens, B. (2014, October). The
 860 distribution and variability of low-level cloud in the North Atlantic trades. *Quar-*
 861 *terly Journal of the Royal Meteorological Society*, *140*(684), 2364–2374. doi:
 862 10.1002/qj.2307
- 863 Nuijens, L., Stevens, B., & Siebesma, A. P. (2009, July). The Environment of Pre-
 864 cipitating Shallow Cumulus Convection. *Journal of the Atmospheric Sciences*,
 865 *66*(7), 1962–1979. doi: 10.1175/2008JAS2841.1
- 866 Rasp, S., Schulz, H., Bony, S., & Stevens, B. (2020, November). Combining Crowd-
 867 sourcing and Deep Learning to Explore the Mesoscale Organization of Shallow
 868 Convection. *Bulletin of the American Meteorological Society*, *101*(11), E1980-
 869 E1995. doi: 10.1175/BAMS-D-19-0324.1
- 870 Raspaud, M., Hoese, D., Lahtinen, P., Dybbroe, A., Finkensieper, S., Roberts, W.,
 871 ... Valentino, A. (2019, June). *Py troll/satpy: Version 0.16.0*. Zenodo. doi:
 872 10.5281/zenodo.3250583
- 873 Rauber, R. M., Ochs, H. T., Di Girolamo, L., Göke, S., Snodgrass, E., Stevens, B.,
 874 ... Twohy, C. H. (2007, December). Rain in Shallow Cumulus Over the Ocean:
 875 The RICO Campaign. *Bulletin of the American Meteorological Society*, *88*(12),
 876 1912–1928. doi: 10.1175/BAMS-88-12-1912
- 877 Riehl, H. (1954). *Tropical meteorology*. McGraw-Hill.
- 878 Saunders, R., Hocking, J., Turner, E., Rayer, P., Rundle, D., Brunel, P., ... Lupu,
 879 C. (2018, July). An update on the RTTOV fast radiative transfer model (cur-
 880 rently at version 12). *Geoscientific Model Development*, *11*(7), 2717–2737. doi:
 881 10.5194/gmd-11-2717-2018
- 882 Schulz, H. (2022, March). C³ONTEXT: A Common Consensus on Convective
 883 OrgaNizaTion during the EUREC⁴A eXperimenT. *Earth System Science Data*,
 884 *14*(3), 1233–1256. doi: 10.5194/essd-14-1233-2022
- 885 Schulz, H., Eastman, R., & Stevens, B. (2021). Characterization and Evolution
 886 of Organized Shallow Convection in the Downstream North Atlantic Trades.
 887 *Journal of Geophysical Research: Atmospheres*, *126*(17), e2021JD034575. doi:
 888 10.1029/2021JD034575
- 889 Seifert, A., & Beheng, K. D. (2006, February). A two-moment cloud microphysics
 890 parameterization for mixed-phase clouds. Part 1: Model description. *Meteorology*

- 891 *and Atmospheric Physics*, 92(1), 45–66. doi: 10.1007/s00703-005-0112-4
- 892 Siebesma, A. P., Bretherton, C. S., Brown, A., Chlond, A., Cuxart, J., Duynkerke,
893 P. G., . . . Stevens, D. E. (2003, May). A Large Eddy Simulation Intercomparison
894 Study of Shallow Cumulus Convection. *Journal of Atmospheric Sciences*, 60(10),
895 1201–1219. doi: 10.1175/1520-0469(2003)60<1201:ALESIS>2.0.CO;2
- 896 Stephan, C. C., Schnitt, S., Schulz, H., Bellenger, H., de Szoeke, S. P., Acquistapace,
897 C., . . . Stevens, B. (2021, February). Ship- and island-based atmospheric sound-
898 ings from the 2020 EUREC⁴A field campaign. *Earth System Science Data*, 13(2),
899 491–514. doi: 10.5194/essd-13-491-2021
- 900 Stevens, B., Ackerman, A. S., Albrecht, B. A., Brown, A. R., Chlond, A., Cuxart,
901 J., . . . Stevens, D. E. (2001, July). Simulations of Trade Wind Cumuli under a
902 Strong Inversion. *Journal of the Atmospheric Sciences*, 58(14), 1870–1891. doi:
903 10.1175/1520-0469(2001)058(1870:SOTWCU)2.0.CO;2
- 904 Stevens, B., Acquistapace, C., Hansen, A., Heinze, R., Klinger, C., Klocke, D., . . .
905 Zängl, G. (2020). The Added Value of Large-eddy and Storm-resolving Models
906 for Simulating Clouds and Precipitation. *Journal of the Meteorological Society of*
907 *Japan. Ser. II*, 98(2), 395–435. doi: 10.2151/jmsj.2020-021
- 908 Stevens, B., Bony, S., Brogniez, H., Hentgen, L., Hohenegger, C., Kiemle, C., . . .
909 Zuidema, P. (2020). Sugar, gravel, fish and flowers: Mesoscale cloud patterns in
910 the trade winds. *Quarterly Journal of the Royal Meteorological Society*, 146(726),
911 141–152. doi: 10.1002/qj.3662
- 912 Stevens, B., Bony, S., Farrell, D., Ament, F., Blyth, A., Fairall, C., . . . Zöger, M.
913 (2021, August). EUREC⁴A. *Earth System Science Data*, 13(8), 4067–4119. doi:
914 10.5194/essd-13-4067-2021
- 915 Stevens, B., Farrell, D., Hirsch, L., Jansen, F., Nuijens, L., Serikov, I., . . . Prospero,
916 J. M. (2016, May). The Barbados Cloud Observatory: Anchoring Investigations
917 of Clouds and Circulation on the Edge of the ITCZ. *Bulletin of the American*
918 *Meteorological Society*, 97(5), 787–801. doi: 10.1175/BAMS-D-14-00247.1
- 919 Stevens, B., Giorgetta, M., Esch, M., Mauritsen, T., Crueger, T., Rast, S., . . .
920 Roeckner, E. (2013). Atmospheric component of the MPI-M Earth System Model:
921 ECHAM6. *Journal of Advances in Modeling Earth Systems*, 5(2), 146–172. doi:
922 10.1002/jame.20015
- 923 Stevens, B., Moeng, C.-H., & Sullivan, P. P. (1999, December). Large-Eddy Sim-

- 924 ulations of Radiatively Driven Convection: Sensitivities to the Representation
 925 of Small Scales. *Journal of the Atmospheric Sciences*, *56*(23), 3963–3984. doi:
 926 10.1175/1520-0469(1999)056<3963:LESORD>2.0.CO;2
- 927 vanZanten, M. C., Stevens, B., Nuijens, L., Siebesma, A. P., Ackerman, A. S., Bur-
 928 net, F., . . . Wyszogrodzki, A. (2011). Controls on precipitation and cloudiness in
 929 simulations of trade-wind cumulus as observed during RICO. *Journal of Advances*
 930 *in Modeling Earth Systems*, *3*(2). doi: 10.1029/2011MS000056
- 931 Vial, J., Vogel, R., Bony, S., Stevens, B., Winker, D. M., Cai, X., . . . Brogniez,
 932 H. (2019, October). A New Look at the Daily Cycle of Trade Wind Cu-
 933 muli. *Journal of Advances in Modeling Earth Systems*, *11*(10), 3148–3166. doi:
 934 10.1029/2019MS001746
- 935 Vial, J., Vogel, R., & Schulz, H. (2021). On the daily cycle of mesoscale cloud or-
 936 ganization in the winter trades. *Quarterly Journal of the Royal Meteorological So-*
 937 *cietly*, *147*(738), 2850–2873. doi: 10.1002/qj.4103
- 938 Vogel, R., Albright, A. L., Vial, J., George, G., Stevens, B., & Bony, S. (2022, De-
 939 cember). Strong cloud–circulation coupling explains weak trade cumulus feedback.
 940 *Nature*, *612*(7941), 696–700. doi: 10.1038/s41586-022-05364-y
- 941 Wan, H., Giorgetta, M. A., Zängl, G., Restelli, M., Majewski, D., Bonaventura,
 942 L., . . . Förstner, J. (2013, June). The ICON-1.2 hydrostatic atmospheric
 943 dynamical core on triangular grids – Part 1: Formulation and performance of
 944 the baseline version. *Geoscientific Model Development*, *6*(3), 735–763. doi:
 945 10.5194/gmd-6-735-2013
- 946 Wick, G. A., Jackson, D. L., & Castro, S. L. (2023, January). Assessing the ability
 947 of satellite sea surface temperature analyses to resolve spatial variability – The
 948 northwest tropical Atlantic ATOMIC region. *Remote Sensing of Environment*,
 949 *284*, 113377. doi: 10.1016/j.rse.2022.113377
- 950 Zängl, G., Reinert, D., Rípodas, P., & Baldauf, M. (2015). The ICON (ICOsahedral
 951 Non-hydrostatic) modelling framework of DWD and MPI-M: Description of the
 952 non-hydrostatic dynamical core. *Quarterly Journal of the Royal Meteorological*
 953 *Society*, *141*(687), 563–579. doi: 10.1002/qj.2378

Supporting Information for ”On the representation of shallow convection in the trades by large-domain, hecto-meter, large-eddy simulations”

Hauke Schulz^{1,2}, Bjorn Stevens¹

¹Max Planck Institute for Meteorology, Hamburg, Germany

²University of Washington/CICOES, Seattle, WA, USA

Contents of this file

1. Figure S1
2. Figure S2
3. Figure S3
4. Figure S4

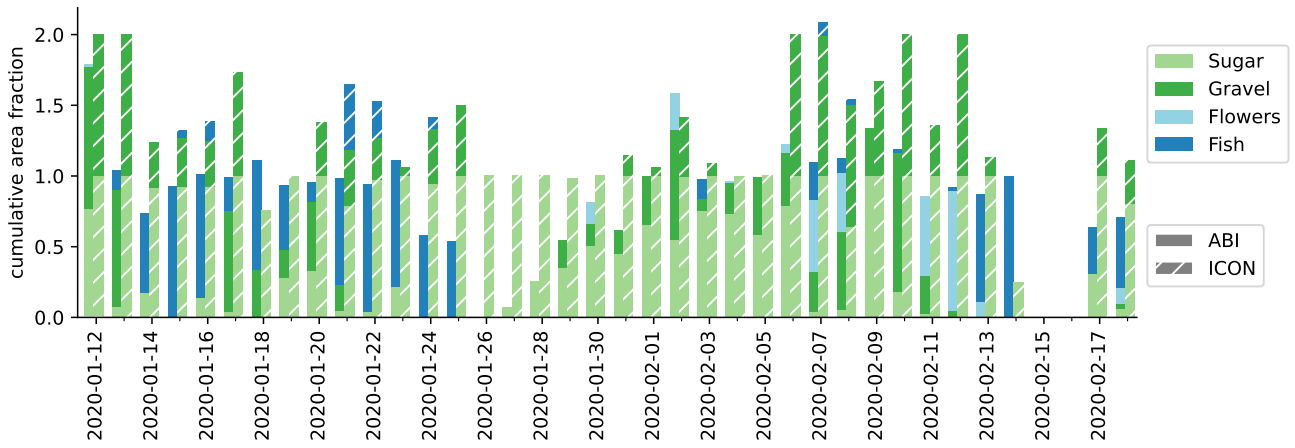


Figure S1. Time-series of mesoscale pattern classifications from the neural network being applied to synthetic satellite images of ICON-312m and actual ABI observations. Cumulative area is calculated as the sum of all pattern classifications and can therefore be above 1 in cases of overlap.

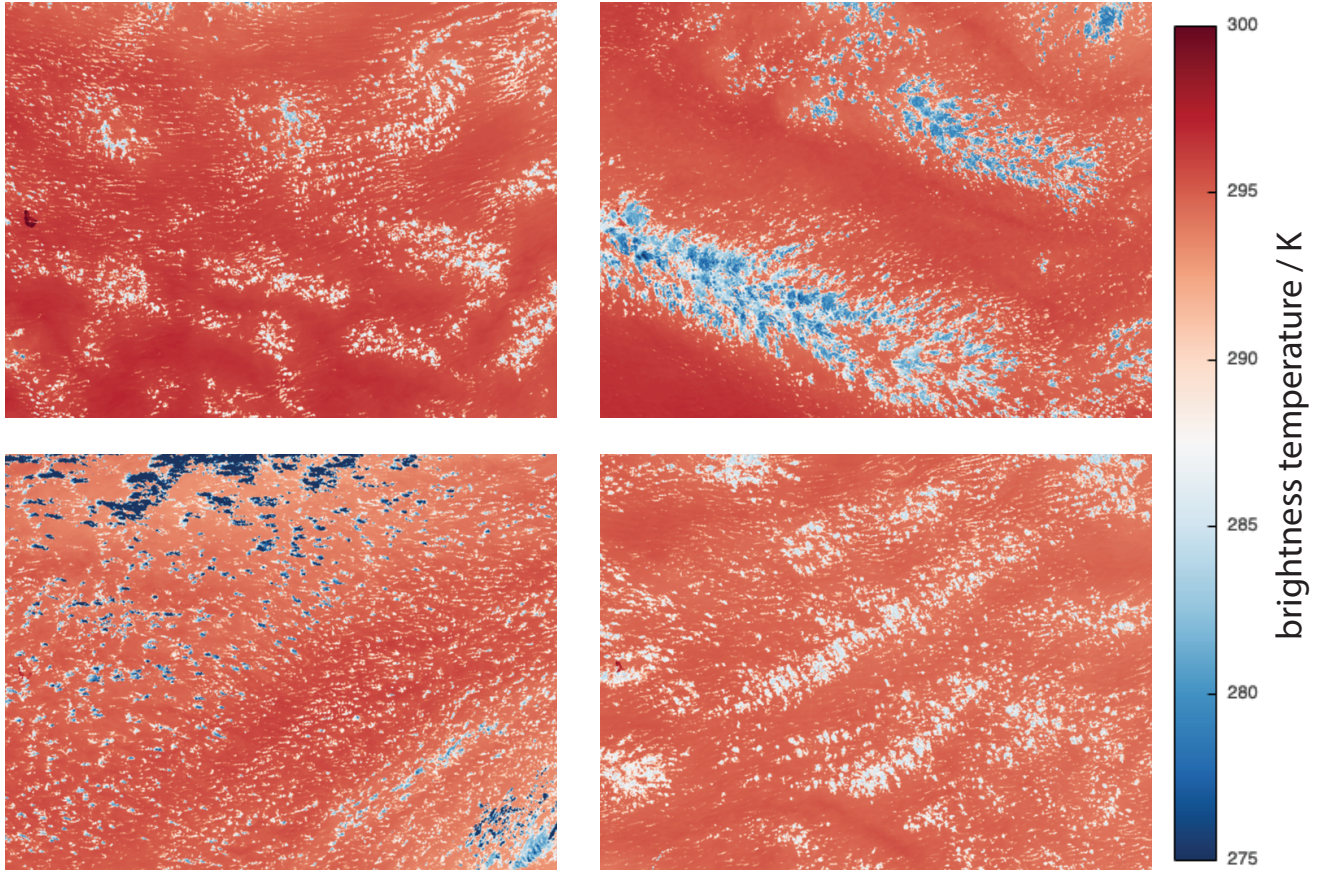


Figure S2. Like Fig. 8b but for the ICON-624m simulation.

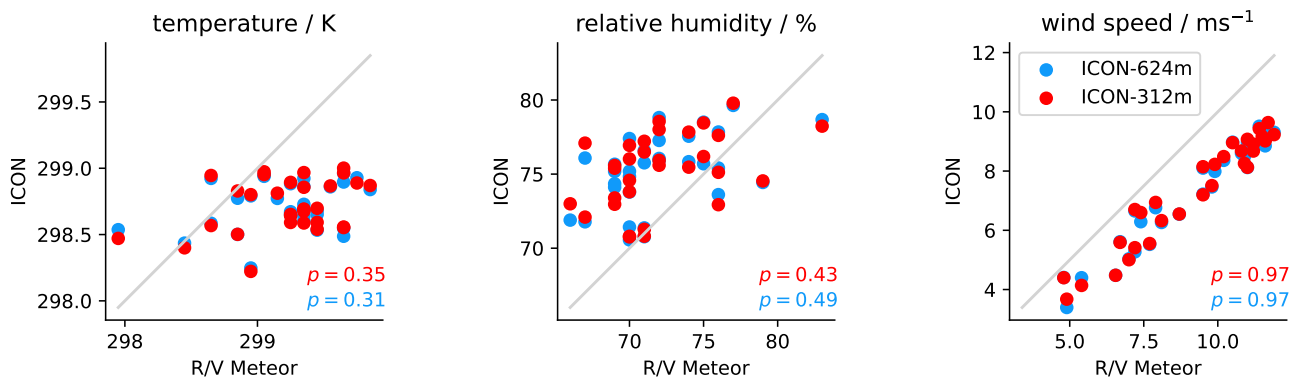


Figure S3. Day-to-day variability of temperature, relative humidity and wind speed based on measurements at the R/V Meteor and the simulation meteogram output at 13.3°N, 56.717°W (eastern circle edge). Grey line indicates the identity line. Pearson correlation coefficients are noted in the bottom right for each simulation with the observations.

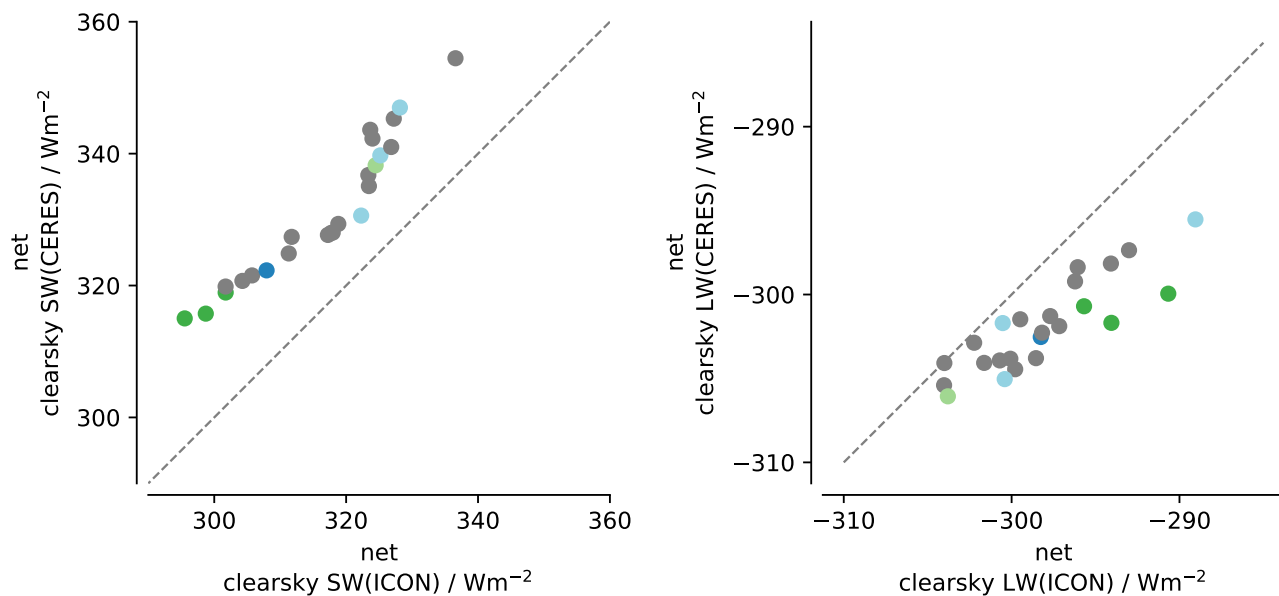


Figure S4. Comparison of day-to-day variability of clear-sky top-of-the-atmosphere radiative flux in the shortwave (left) and longwave(right) between CERES and ICON-312m for days without high clouds as in Fig.18. The mean differences between the observed and simulated fluxes are -15 W m^{-2} and 4 W m^{-2} for the shortwave and longwave, respectively.